Single nuclei transcriptomics reveal the differentiation trajectories of periosteal skeletal/stem progenitor cells in bone regeneration

Simon Perrin[1], Maria Ethel[1], Vincent Bretegnier[1], Cassandre Goachet[1], Cécile-Aurore Wotawa[1], Marine Luka[2,3], Fanny Coulpier[1], Cécile Masson[4,5], Mickael Ménager[2,3], and Céline Colnot[1,*]

[1] Univ Paris Est Creteil, INSERM, IMRB, Creteil, France

[2]Paris Cité University, Imagine Institute, Laboratory of Inflammatory Responses and Transcriptomic Networks in Diseases, Atip-Avenir Team, INSERM UMR 1163, Paris, France.

[3] Labtech Single-Cell@Imagine, Imagine Institute, INSERM UMR 1163, Paris, France.

[4] Bioinformatics Core Facility, Institut Imagine-Structure Fédérative de Recherche Necker, INSERM U1163

[5] INSERM US24/CNRS UAR3633, Paris Cité University, Paris, France

*Corresponding author: celine.colnot@inserm.fr, +33 1 49 81 39 55

Abstract

Bone regeneration is mediated by skeletal stem/progenitor cells (SSPCs) that are mainly recruited from the periosteum after bone injury. The composition of the periosteum and the steps of SSPC activation and differentiation remain poorly understood. Here, we generated a single-nuclei atlas of the periosteum at steady-state and of the fracture site during early stages of bone repair (https://fracture-repair-atlas.cells.ucsc.edu). We identified periosteal SSPCs expressing stemness markers (*Pi16* and *Ly6a*/SCA1) and responding to fracture by adopting an injury-induced fibrogenic cell (IIFC) fate, prior to undergoing osteogenesis or chondrogenesis. We identified distinct gene cores associated with IIFCs and their engagement into osteogenesis and chondrogenesis involving Notch, Wnt and the circadian clock signaling respectively. Finally, we show that IIFCs are the main source of paracrine signals in the fracture environment, suggesting a crucial paracrine role of this transient IIFC population during fracture healing. Overall, our study provides a complete temporal topography of the early stages of fracture healing and the dynamic response of periosteal SSPCs to injury, redefining our knowledge of bone regeneration.

Graphical Abstract

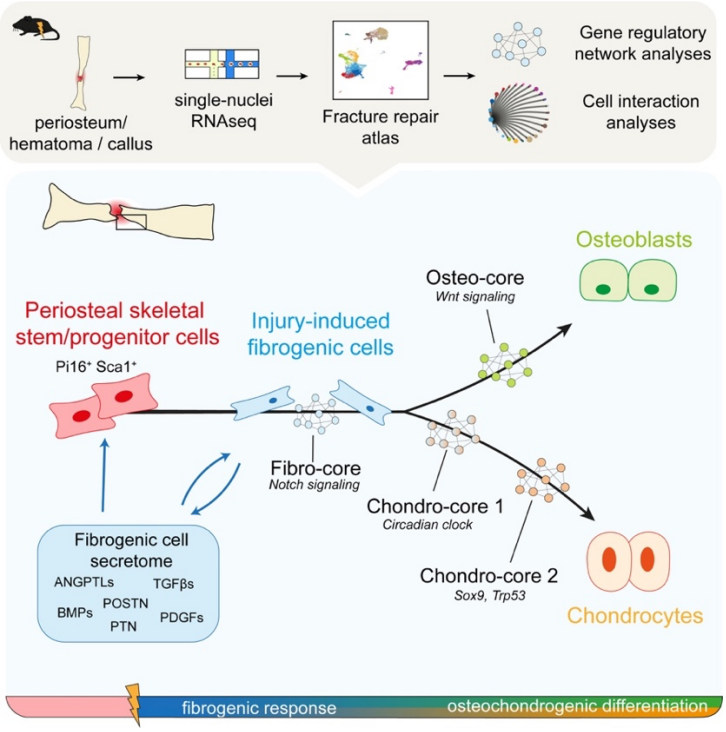

Keywords

periosteum – bone repair – skeletal stem/progenitor cells – single nuclei RNAseq

Introduction

The skeleton provides structural support and protection for internal organs in the vertebrate body. Bones can fracture but regenerate themselves efficiently without scarring. Bone regeneration is mediated by the action of resident skeletal stem/progenitor cells (SSPCs) from periosteum and bone marrow, and SSPCs from skeletal muscle adjacent to the fracture site[1–4]. SSPCs are activated during the inflammatory phase of healing and differentiate into osteoblasts and/or chondrocytes to repair bone via a combination of intramembranous and endochondral ossification. During intramembranous ossification SSPCs differentiate directly into osteoblasts, while during endochondral ossification SSPCs first differentiate into chondrocytes to form an intermediate cartilage template subsequently replaced by bone.

The periosteum, an heterogeneous tissue located on the outer surface of bones, is a crucial source of SSPCs during bone healing[1,2,5–7]. Periosteal SSPCs exhibit a high regenerative potential. They also display both osteogenic and chondrogenic potentials after injury compared to bone marrow SSPCs that are mostly osteogenic and skeletal muscle SSPCs that are mostly chondrogenic[1–4,8]. Periosteal SSPCs (pSSPCs) are still poorly characterized and their response to bone injury remain elusive. Recent advances in single cell/nuclei transcriptomic analyses provided new insights in stem cell population heterogeneity and regeneration processes in many organs[9–11]. However, few studies have investigated bone fracture healing at the single cell level and these studies have focused on cultured cells or late stages of bone repair[3,12]. Therefore, a complete dataset of periosteum and bone regeneration is lacking and is essential to decipher the mechanisms of pSSPC activation and regulation. Here, we created a single-nuclei atlas of the uninjured periosteum and its response to bone fracture. We generated single-nuclei RNAseq (snRNAseq) datasets from the uninjured periosteum and from the periosteum and hematoma/callus at days 3, 5 and 7 post-tibial fracture. Our analyses thoroughly describe the heterogeneity of the periosteum at steady state and the steps of pSSPC activation and differentiation after injury. We show that pSSPCs represent a single population localized in the fibrous layer of the periosteum. Periosteal SSPCs can provide

60 osteoblasts and chondrocytes for bone repair by first generating a common injury-induced
61 fibrogenic cell (IIFC) population that can then engage into osteogenesis and chondrogenesis.
62 We identified the gene networks regulating pSSPC fate after injury and IIFCs as the main
63 population producing paracrine factors mediating the initiation of bone healing.

Results

Heterogeneity of the periosteum at steady state

To investigate the heterogeneity of the periosteum at steady-state, we performed snRNAseq of the periosteum of wild-type mice (Fig. 1A-B). Single nuclei transcriptomics was previously shown to provide results equivalent to single cell transcriptomics, but with better cell type representation and reduced digestion-induced stress response[13–16]. After filtering, we obtained 1189 nuclei, corresponding to 8 cell populations: SSPC (expressing *Pi16*), fibroblasts (expressing *Pdgfra*), osteogenic cells (expressing *Runx2*), Schwann cells (expressing *Mpz*), pericytes/SMC (expressing *Tagln*), immune cells (expressing *Ptprc*), adipocytes (expressing *Lpl*), and endothelial cells (ECs, expressing *Pecam1*) (Fig. 1C-D, Fig. 1 – Supplementary Figure 1A). We performed in depth analyses of the SSPC, fibroblast and osteogenic cell populations. Subset analyses of clusters 0 to 5 identified 5 distinct SSPC/fibroblast populations expressing *Pdgfra* and *Prrx1*: *Pi16*$^+$ *Ly6a* (SCA1)$^+$ cells (cluster 0), *Csmd1*$^+$ cells (cluster 1), *Hsd11b1*$^+$ cells (cluster 2), *Cldn1*$^+$ cells (cluster 3), and *Luzp2*$^+$ cells (cluster 4) (Fig. 2A-B). Cluster 0 is the only cell cluster containing cells expressing *Pi16*$^+$ and stemness markers including *Ly6a* (SCA1), *Dpp4,* and *Cd34* (Fig. 2C-D). Cytotrace scoring identified *Pi16*$^+$ cells as the population in the most undifferentiated state (Fig. 2E). We performed in vitro CFU assays with sorted GFP$^+$SCA1$^+$ and GFP$^+$SCA1$^-$ cells isolated from the periosteum of *Prx1*^{Cre}*; R26*^{mTmG} mice, as *Prx1* labels all SSPCs contributing to the callus formation including *Pi16*$^+$ cells (Fig 2D) [1]. Prx1-GFP$^+$ SCA1$^+$ cells showed higher CFU potential compared to GFP$^+$SCA1$^-$ cells, confirming their stem/progenitor property (Fig 2F-G). Then, we grafted Prx1-GFP$^+$ SCA1$^+$ et Prx1-GFP$^+$ SCA1$^-$ periosteal cells at the fracture site of wild-type mice. Only GFP$^+$SCA1$^+$ cells formed cartilage after fracture indicating that GFP$^+$SCA1$^+$ cells encompass periosteal SSPCs with osteochondrogenic potential (Fig 2H). We explored the expression of other known markers of periosteal SSPCs, including *Ctsk*, *Acta2* (αSMA), *Gli1*, and *Mx1*, but no marker was fully specific to one cell cluster (Fig. 2 – Supplementary Fig. 1) [1,2,5–7,17–21].

91 **The fracture repair atlas**

92 To investigate the periosteal response to bone fracture, we collected injured periosteum with
93 hematoma or callus at days 3, 5 and 7 post-fracture, extracted the nuclei and processed them for
94 snRNAseq (Fig. 3A). We combined the datasets with the uninjured periosteum from Figure 1 and
95 obtained a total of 6213 nuclei after filtering. The combined dataset was composed of 25 clusters
96 corresponding to 11 cell populations: SSPCs (expressing *Pi16*), injury-induced fibrogenic cells
97 (IIFCs, expressing ECM-related genes including *Postn*), osteoblasts (expressing *Ibsp*),
98 chondrocytes (expressing *Col2a1*), osteoclasts (expressing *Ctsk*), immune cells (expressing
99 *Ptprc*), Schwann cells (expressing *Mpz*), endothelial cells (expressing *Pecam1*), pericytes
100 (expressing *Rgs5*), SMCs (expressing *Tagln*) and adipocytes (expressing *Lpl*) (Fig. 3B-C, Fig 3 –
101 Supplementary Fig. 1-2). Next, we observed the dynamics of the cell populations in response to
102 bone fracture (Fig. 3D, Fig 3 – Supplementary Fig. 1B). After injury, the percentage of SSPCs was
103 strongly decreased and the percentage of IIFCs progressively increased (Fig. 3D-E). The
104 percentage of chondrocytes and osteoblasts increased from day 3 post-fracture. Immune cells
105 were drastically increased at day 3 after injury, before progressively decreasing at days 5 and 7
106 post-fracture (Fig. 3E).

107

108 **Spatial organization of the fracture callus**

109 To evaluate the spatial distribution of the main cell populations identified in the snRNAseq datasets,
110 we performed in situ immunofluorescence and RNAscope experiments on uninjured periosteum
111 and days 3, 5 and 7 post-fracture hematoma/callus tissues. In the uninjured periosteum, we
112 detected *Pi16*-expressing SSPCs, *Postn*-expressing cells, OSX^+ osteoblasts, $CD31^+$ endothelial
113 cells and $CD45^+$ immune cells (Fig 4A-B). *Pi16*-expressing SSPCs were located within the fibrous
114 layer, while *Postn*-expressing cells were found in the cambium layer and corresponded to *Runx2*-
115 expressing osteogenic cells (Fig. 4 – Supplementary Fig. 1A-C). Although *Postn* expression was
116 weak in uninjured periosteum, *Postn* expression was strongly increased in response to fracture,
117 specifically in IIFCs (Fig. 4 – Supplementary Fig. 1D-E). At day 3 post-fracture, we observed
118 periosteal thickening and the formation of a fibrous hematoma (Fig. 4C). We did not detect *Pi16*-
119 expressing SPPCs, consistent with the absence of cells expressing SSPC markers in the day 3

120 snRNAseq dataset compared to uninjured periosteum (Fig. 4 – Supplementary Figure 2). POSTN$^+$
121 IIFCs and immune cells were the main populations present in hematoma and activated periosteum.
122 Few IIFCs in the activated periosteum expressed SOX9 and OSX and only the periosteum was
123 vascularized (Fig. 4D). At days 5 and 7 post-fracture, the callus was formed mainly of fibrotic tissue,
124 new bone formed on the periosteal surface at the periphery of the callus and small cartilage islets
125 were detected in the center of the callus near the periosteal surface (Fig. 4E-H). The fibrotic tissue
126 contained mostly IIFCs, as well as immune and endothelial cells. We also observed SOX9$^+$ and
127 OSX$^+$ cells in the fibrotic tissue, while the cartilage was solely composed of SOX9$^+$ chondrocytes.
128 OSX$^+$ osteoblasts were the main cell population detected in the new bone at the periosteal surface.
129 We also observed a progressive reduction of POSTN$^+$ cells and immune cells from day 5 to 7 and
130 increased vascularization in the newly formed bone (Fig. 4E-H).
131
132 **Periosteal SSPCs differentiate via an injury-induced fibrogenic stage**
133 To understand the differentiation and fate of pSSPCs after fracture, we analyzed the subset of
134 SSPC, IIFC, chondrocyte and osteoblast clusters from the combined fracture dataset (Fig. 5A, Fig.
135 5 – Supplementary Figure 1). We performed pseudotime analyses to determine the differentiation
136 trajectories, defining the starting point in the pSSPC population, where the uninjured and
137 undifferentiated cells cluster. We identified that pSSPCs differentiate in 3 stages starting from the
138 pSSPC population (expressing *Ly6a*, *Pi16* and *Cd34*), predominant in uninjured dataset (Fig. 5B-
139 C). Periosteal SSPCs then transition through an injury-induced fibrogenic stage predominant at
140 days 3 and 5 post-injury. In this intermediate fibrogenic stage, IIFCs express high levels of
141 extracellular matrix genes, such as *Postn*, *Aspn* and collagens. Subsequently, IIFCs differentiate
142 into chondrocytes (expressing *Acan*, *Col2a1* and *Sox9*) or osteoblasts (expressing *Sp7*, *Alpl* and
143 *Ibsp*), both predominant at days 5 and 7 (Fig. 5B-C, Table S1). We observed a parallel between
144 pseudotime and the timepoints of the dataset, confirming that the differentiation trajectory follows
145 the timing of cell differentiation (Fig. 5D). These results show that pSSPCs respond to fracture via
146 an injury-induced fibrogenic stage common to chondrogenesis and osteogenesis and independent
147 of their final fate (Fig. 5E). To visualize the transition of IIFCs towards chondrocytes and osteoblasts
148 in the fracture callus, we performed co-immunofluorescence on day 5 post-fracture

149 hematoma/callus. We observed a progressive increase in SOX9 and OSX signals in IIFCs at the
150 fibrosis-to-cartilage and fibrosis-to-bone transition zones respectively (Fig 6A). To functionally
151 validate the steps of pSSPC activation, we isolated SCA1$^+$ GFP$^+$ pSSPCs from *Prx1^{Cre}; R26^{mTmG}*
152 mice, excluding endothelial cells (SCA1$^+$GFP$^-$) and pericytes (SCA1$^-$GFP$^+$), and grafted them at
153 the fracture site of wild-type hosts (Fig. 6B, Figure 6 – Supplementary Figure 1). We observed that
154 grafted GFP$^+$ pSSPCs formed POSTN$^+$ IIFCs at day 5 post-fracture (Fig 6B). Then, we isolated
155 IIFCs, that correspond to GFP$^+$ CD146$^-$ cells from the day 3 post-fracture callus of *Prx1^{Cre}; R26^{mTmG}*
156 mice without contamination by pericytes (GFP$^+$CD146$^+$ cells) (Fig. 6C, Figure 6 – Supplementary
157 Figure 1). We grafted the GFP+ IIFCs at the fracture site of wild-type hosts and showed that grafted
158 cells formed bone and cartilage at day 14 post-fracture. These results confirmed that pSSPCs first
159 become IIFCs that differentiate into osteoblasts and chondrocytes.
160
161 **Characterization of injury-induced fibrogenic cells**
162 We performed in depth analyses of the newly identified IIFC population. Gene ontology (GO)
163 analyses of upregulated genes in IIFCs (clusters 2 to 6) showed enrichment in GOs related to
164 tissue development, extracellular matrix (ECM), and ossification (Fig. 7A). We identified several
165 ECM-related genes specifically upregulated in IIFCs, including collagens (*Col3a1, Col5a1, Col8a1,*
166 *Col12a1*), *Postn*, and *Aspn* (Fig. 7B-C, Fig. 7 – Supplementary Figure 1). We also identified GO
167 terms related to cell signaling, migration, differentiation, and proliferation, indicating that this step
168 corresponds to an injury response. Only a small subset of IIFCs undergo apoptosis, further
169 supporting that IIFCs are maintained in the fracture environment giving rise to osteoblasts and
170 chondrocytes (Fig. 7 – Supplementary Figure 2). To further understand the mechanisms regulating
171 SSPC activation and fate after injury, we performed gene regulatory network (GRN) analyses on
172 the subset of SSPCs, IIFCs, osteoblasts and chondrocytes using SCENIC package (Single Cell
173 rEgulatory Network Inference and Clustering)[22]. We identified 280 activated regulons (transcription
174 factor/TF and their target genes) in the subset dataset. We performed GRN-based tSNE clustering
175 and identified SSPC, IIFC, chondrocyte and osteoblast populations (Fig. 7D-E, Fig. 7-
176 Supplementary Figure 3A). Fibroblasts from uninjured periosteum (*Hsd11b1$^+$, Cldn1$^+$* and *Luzp2$^+$*
177 cells and corresponding to cluster 10 of Fig. 5B) clustered separately from the other populations,

178 suggesting the absence of their contribution to bone healing. Analysis of the number of activated
179 regulons per cell indicated that SSPCs are the most stable cell population (higher number of
180 activated regulons), while IIFCs are the less stable population, confirming their transient state (Fig.
181 7F). We then investigated cell population specific regulons. SSPCs showed activated regulons
182 linked to stemness, including Hoxa10 (16g), Klf4 (346g), Pitx1 (10g), and Mta3 (228g) [23–25], and
183 immune response, including Stat6 (30g), Fiz1 (72g) and Stat5b (18g)[26–28] (Fig. 7G). Osteoblasts
184 and chondrocytes display cell specific activated regulons including Sp7 (18g) and Sox9 (77g)
185 respectively. We identified 21 regulons that we named fibro-core and that were upregulated
186 specifically in the IIFC population (Fig. 7H-I, Table S2). Several fibro-core regulons, such as Meis1
187 (1556g), Pbx1 (11g), Six1 (20g), and Pbx3 (188g) are known to be involved in cell differentiation
188 during tissue development and repair[29–32]. Reactome pathway analysis showed that the most
189 significant terms linked to IIFC-specific TFs are related to Notch signaling (Fig. 7J, Table S3). We
190 confirmed that Notch signaling is increased in the IIFC stage (Fig. 7J), suggesting its involvement
191 in the fibrogenic phase of bone repair.
192
193 **Distinct gene cores regulate the engagement of IIFCs in chondrogenesis and osteogenesis**
194 We sought to identify the drivers of the transition of IIFCs to chondrocytes or osteoblasts. We
195 identified 2 cores of regulons involved in chondrogenic differentiation. Chondro-core 1 is composed
196 of 9 regulons specific to the transition of IIFCs to chondrocytes, including Maf (17g), Arntl (1198g),
197 and Nfatc2 (37g) and chondro-core 2, composed of 14 regulons specific to differentiated
198 chondrocytes (Fig. 8A, Fig. 8- Supplementary Figure 1A). Chondro-core 1 regulons are known to
199 be regulators of the circadian clock (Npas2, Arntl) or of the T/B-cell receptor cellular response
200 (Bach2, Nfact2, Nfkb1). STRING network analysis showed that TFs from the chondro-core 1 are
201 interacting between each other and are at the center of the interactions between the chondro-core
202 2 TFs, including Sox9, Trp53 and Mef2c (Fig. 8B, Fig. 8- Supplementary Figure 1B). We observed
203 that chondro-core 1 is only transiently activated when IIFCs are engaging into chondrogenesis and
204 precedes the activation of chondro-core 2 (Fig. 8C-D). Chondro-core 1 activity was high in early
205 differentiated chondrocytes (low *Acan* expression) and progressively reduced as chondrocytes
206 undergo differentiation, while chondro-core 2 activity was gradually increased as chondrocytes

207 differentiate (Fig. 8D). This suggests that transient activation of the chondro-core 1 allows the
208 transition of IIFCs into chondrocytes. Then, we investigated the osteogenic commitment of IIFCs.
209 We identified 8 regulons forming the osteo-core and activated in IIFCs transitioning to osteoblasts,
210 such as Tcf7 (23g), Bcl11b (14g), and Tbx2 (36g) (Fig. 8E, Fig. 8- Supplementary Figure 1C).
211 STRING network analysis showed that the genes with the strongest interaction with the osteo-core
212 TFs are mostly related to Wnt signaling (Fig. 8F). This reveals the role of Wnt signaling in this
213 transition from early fibrogenic activation of pSSPCs to osteogenic differentiation during bone
214 repair. We calculated the osteo-core activity and observed that it is gradually increased and
215 maintained in osteogenic cells, showing that the osteo-core is required for the transition and
216 maturation of IIFC into osteoblasts (Fig 8G-H). Overall, we identified distinct cores of regulons with
217 distinct dynamics driving the transition of IIFCs into chondrocytes and osteoblasts.
218
219 **IIFCs mediate paracrine interactions during bone repair**
220 Paracrine cell interactions are crucial drivers of tissue regeneration and stem cell activation. To
221 identify key cell interactions during bone repair, we performed cell interaction analyses using
222 CellChat package[33]. We observed that IIFCs are one of the predominant sources of outgoing
223 signals during bone repair, and are also important receivers of signals, suggesting their central role
224 in mediating cell interactions after fracture (Fig. 9A-B). Endothelial cells were mostly receiving
225 signaling, while chondrocytes, osteoblasts and most immune cells exhibited reduced interactions
226 with the other cell types in the fracture environment. IIFCs interact with all cell populations in the
227 fracture environment, but the strongest interactions were with SSPCs and IIFCs (Fig. 9-
228 Supplementary Figure 1A). CellChat analyses of the subset of SSPCs, IIFCs, osteoblasts and
229 chondrocytes confirmed that IIFCs are a major source and receiver population of paracrine signals
230 after fracture (Fig. 9- Supplementary Figure 1B). We then analyzed the main secreted factors from
231 IIFCs. IIFCs secreted periostin (*Postn*), BMPs (*Bmp5*), pleiotropin/PTN (*Ptn*), TGFβs (*Tgfb2*,
232 *Tgfb3*), PDGFs (*Pdgfc*, *Pdgfd*) and angiopoietin-likes/ANGPTLs (*Angplt2, Angplt4*) (Fig. 9C-D, Fig.
233 9- Supplementary Figure 1C). We observed differences in the dynamics of these factors, as some
234 of them peak at day 3 post-fracture such as TGFβ, while others peak at day 5 such as BMP,
235 POSTN, PTN and ANGPLT (Fig. 9E). We assessed the dynamics of ligand and receptor expression

236 and observed that ligand expression was increased during the IIFC phase and specific of the
237 fracture response (Fig. 9F). Receptor expression was high in both SSPCs and IIFCs, and receptors
238 were expressed from steady state, suggesting that SSPCs can receive signals from IIFCs. Analysis
239 of SSPC incoming signals showed that IIFCs produce paracrine factors that can regulate SSPCs
240 (Fig. 9G), indicating that they contribute to SSPC recruitment after fracture.

Discussion

The periosteum is the main driver of bone regeneration. Yet the periosteum composition and its response to bone fracture are poorly described. Here, we used single-nuclei transcriptomics to understand the heterogeneity of the periosteum at steady state and the changes occurring within the periosteum after bone fracture. We developed a protocol to extract nuclei from freshly dissected periosteum, allowing us to capture their intact transcriptomic profile without enzymatic digestion-induced stress[13,34,35]. In addition, we performed snRNAseq without sorting specific populations, allowing the identification of all cell types located in the periosteum and the fracture environment from the early stages of repair. Our study provides the first complete fracture repair atlas, a key tool to understand bone regeneration.

First, we described the heterogeneity of the periosteum at steady state. While previous studies performed scRNAseq on sorted periosteal cell populations, our dataset uncovers the diversity of cell populations within the periosteum. We describe fibroblast populations, as well as tissue resident immune cells, adipocytes, and blood vessel/nerve-related cells. We identified one SSPC population of undifferentiated cells localized in the fibrous layer of the periosteum and expressing markers such as SCA1, *Dpp4* and *Pi16,* known to mark fibroblasts with stemness potential[36]. No markers previously described such as *Ctsk*, or *Gli1* were fully specific of one cell cluster and of the undifferentiated SSPC population, suggesting that these markers may label heterogeneous cell populations[2,5,6,19].

After fracture, the composition of the periosteum changes drastically, with the appearance of IIFC and immune cells from day 3 post-fracture, and of chondrocytes and osteoblasts from day 5 post-fracture. Previous studies based on in vitro analyses and in vivo lineage tracing demonstrated that the periosteum displays the unique potential to form both bone and cartilage after fracture[1,3,5]. Yet, it was still unknown if the periosteum contains a bipotent SSPC population or several SSPC populations with distinct potentials after injury. Here, we show that pSSPCs respond to injury and form bone and cartilage via a single trajectory emerging from SCA1^{+} SSPCs. Periosteal SCA1^{+} SSPCs become IIFCs, a state marked by a decreased expression of stemness markers and a

271 strong expression of extracellular matrix genes, such as *Postn* and *Aspn* and activation of Notch-
272 related TFs. Thus, bone injury does not induce an expansion of SCA1^{+} SSPCs, rather a transition
273 toward IIFCs that progressively expand and represent the main cell population within the fracture
274 callus until day 7 post-fracture. Following this fibrogenic step, IIFCs do not undergo cell death but
275 undergo either osteogenesis or chondrogenesis. This newly identified transient IIFC state
276 represents the crossroad of bone regeneration and SSPC differentiation. In tissues such as skeletal
277 muscle, an early transient fibrogenic response is also required for regeneration supporting muscle
278 stem cell activation and differentiation[37]. During bone repair, this initial fibrogenic process is an
279 integral part of the SSPC differentiation process, and a transitional step prior to osteogenesis and
280 chondrogenesis.
281
282 GRN analyses identified TFs regulating SSPC response to fracture and involved in several cardinal
283 signaling pathways including Notch and Wnt. Previous studies reported the role of Notch and Wnt
284 in bone repair [8,38–48]. Notch inactivation at early stages of repair leads to bone non-union while
285 Notch inactivation in chondrocytes and osteoblasts does not significantly affect healing, correlating
286 with our data showing that Notch is crucial during the IIFC phase, prior to osteochondral
287 commitment[39]. Our results show that Wnt activation occurs after Notch activation and is specific to
288 IIFCs engaging into osteogenesis, confirming its crucial role as a regulator of osteogenesis [8,45–48].
289 In addition, we identified a chondro-core of 9 regulons transiently activated when IIFCs engage into
290 chondrogenesis. Among these regulons, several are involved in the autonomous circadian clock,
291 including *Npas2* and *Arntl* (Bmal1). Bmal1 was previously shown to be a regulator of cartilage
292 differentiation in bone development and homeostasis[49]. Bmal1 inactivation leads to chondrocyte
293 apoptosis and disruption of signaling involved in cartilage formation, including TGFβ, Ihh, HIF1α
294 and NFAT[50–53]. This suggests a role of the circadian clock genes as key regulators of
295 chondrogenesis during bone repair. IIFCs are also revealed as crucial paracrine regulators of the
296 fracture environment. IIFCs secrete factors including BMPs, PDGFs, TGFβs, and POSTN, known
297 to be required for successful bone healing[1,3,18,54]. These signals potentially regulate the interactions
298 between IIFCs and all other cell types in the fracture environment, but primarily SSPCs and IIFCs

299 themselves. Thus, IIFCs appear to contribute to the recruitment of SSPCs and promote their own
300 maturation and differentiation.
301
302 Overall, our study provides a complete dataset of the early steps of bone regeneration. The newly
303 identified SSPC activation pattern involves a coordinated temporal dynamic of cell phenotypes and
304 signaling pathways after injury. IIFCs emerge as a transient cell population that plays essential
305 roles in the initial steps of bone repair. Deeper understanding of IIFC regulation will be crucial as
306 they represent the ideal target to enhance bone healing and potentially treat bone repair defects.
307

Materials and Methods

Mice

C57BL/6ScNj were obtained from Janvier Labs (France). *Prx1*^{Cre} [55] and *Rosa26-mtdTomato-mEGFP* (*R26*^{mTmG})[56] were obtained from Jackson Laboratory (Bar Harbor, ME).). All SSPCs, including pSSPCs, are marked by GFP in *Prx1*$^{Cre;}$ R26^{mTmG} mice. Mice were bred in animal facilities at IMRB, Creteil and kept in separated ventilated cages, in pathogen-controlled environment and ad libitum access to water and food. All procedures performed were approved by the Paris Est Creteil University Ethical Committee. Twelve-week-old males and females were mixed in experimental groups.

Tibial fracture

Open non-stabilized tibial fractures were induced as previously described [57]. Mice were anesthetized with an intraperitoneal injection of Ketamine (50 mg/mL) and Medetomidine (1 mg/kg) and received a subcutaneous injection of Buprenorphine (0.1 mg/kg) for analgesia. Mice were kept on a 37°C heating pad during anesthesia. The right hindlimb was shaved and sanitized. The skin was incised to expose the tibia and osteotomy was performed in the mid-diaphysis by cutting the bone. The wound was sutured, the mice were revived with an intraperitoneal injection of atipamezole (1 mg/kg) and received two additional analgesic injections in the 24 hours following surgery. Mice were sacrificed at 3, 5, 7 or 14 days post-fracture.

Nuclei extraction

Nuclei extraction protocol was adapted from [58,59]. We generated 4 datasets for this study: uninjured periosteum, periosteum and hematoma at days 3, 5 and 7 post-tibial fracture. The uninjured and day 3 post-fracture datasets were generated in duplicates. For uninjured periosteum, tibias from 4 mice were dissected free of muscle and surrounding tissues. The epiphyses were cut and the bone marrow flushed. The periosteum was scraped from the cortex using dissecting Chisel (10095-12, Fine Science Tools). For days 3, 5 and 7 post fracture, injured tibias from 4 to 9 mice were collected and the surrounded tissues were removed. The activated periosteum was scraped and collected with the hematoma. Collected tissues were minced and placed 5 min in ice-cold Nuclei Buffer

337 (NUC101, Merck) before mechanical nuclei extraction using a glass douncer. Extraction was
338 performed by 20 strokes of pestle A followed by 5-10 of pestle B. Nuclei suspension was filtered,
339 centrifuged and resuspended in RNAse-free PBS (AM9624, ThermoFischer Scientific) with 2%
340 Bovine Serum Albumin (A2153, Merck) and 0.2 U/µL RNAse inhibitor (3335399001, Roche). A
341 second step of centrifugation was performed to reduce contamination by cytoplasmic RNA. Sytox™
342 AADvanced™ (S10349, ThermoFischer Scientific) was added (1/200) to label nuclei and Sytox-
343 AAD+ nuclei were sorted using Sony SH800.
344
345 **Single nuclei RNA sequencing**
346 The snRNA-seq libraries were generated using Chromium Single Cell Next GEM 3′ Library & Gel
347 Bead Kit v.3.1 (10x Genomics) according to the manufacturer's protocol. Briefly, 10 000 to 20 000
348 nuclei were loaded in the 10x Chromium Controller to generate single-nuclei gel-beads in emulsion.
349 After reverse transcription, gel-beads in emulsion were disrupted. Barcoded complementary DNA
350 was isolated and amplified by PCR. Following fragmentation, end repair and A-tailing, sample
351 indexes were added during index PCR. The purified libraries were sequenced on a Novaseq
352 (Illumina) with 28 cycles of read 1, 8 cycles of i7 index and 91 cycles of read 2. Sequencing data
353 were processed using the Cell Ranger Count pipeline and reads were mapped on the mm10
354 reference mouse genome with intronic and exonic sequences.
355
356 **Filtering and clustering using Seurat**
357 Single-nuclei RNAseq analyses were performed using Seurat v4.1.0 [60,61] and Rstudio v1.4.1717.
358 Aligned snRNAseq datasets were filtered to retain only nuclei expressing between 200 et 5000
359 genes and expressing less than 2% of mitochondrial genes and 1.5% of ribosomal genes.
360 Contamination from myogenic cells were removed from the analyses. After filtering, we obtained
361 1378 nuclei from uninjured periosteum, 1634 from day 3 post-fracture, 2089 from d5 post-fracture
362 and 1112 from day 7 post-fracture. The replicates of the uninjured dataset were integrated using
363 Seurat. The integrated dataset was regressed on cell cycle, mitochondrial and ribosomal content
364 and clustering was performed using the first 15 principal components and a resolution of 0.5.
365 SSPC/fibroblast and osteogenic cells were isolated and reclustered using the first 10 principal

366 components and a resolution of 0.2. Uninjured, d3, d5 and d7 datasets were integrated using
367 Seurat. The integrated dataset was regressed on cell cycle, mitochondrial and ribosomal content.
368 Clustering was performed using the first 20 principal components and a resolution of 1.3. SSPC,
369 IIFC, chondrogenic and osteogenic clusters from the integration were isolated to perform subset
370 analysis. The subset was reclustered using the first 15 principal components and a resolution of
371 0.6.
372

373 **Pseudotime analysis using monocle3**

374 Monocle3 v1.0.0 was used for pseudotime analysis [62]. Single-cell trajectories were determined
375 using monocle3 default parameters. The starting point of the pseudotime trajectory was determined
376 as the cells from the uninjured dataset with the highest expression of stem/progenitor marker genes
377 *(Ly6a, Cd34, Dpp4, Pi16)*. Pseudotime values were added in the Seurat object as metadata and
378 used with the Seurat package.
379

380 **Differentiation state analysis using Cytrotrace**

381 To assess the level of differentiation of the cell clusters, we performed analyses using CytoTrace
382 with the default parameters. Cytotrace scoring was plotted in violin plot and on the Seurat UMAP
383 clustering.
384

385 **Gene Ontology and Reactome and analyses**

386 Reactome and GO analyses were performed using EnrichR [63]. All significant GO terms from
387 upregulated genes in clusters 2 to 6 of the subset of SSPCs, IIFCs, osteoblasts and chondrocytes
388 were manually categorized. The 5 more significant terms of the Reactome analysis from the
389 fibrogenic TFs of Fig. 6 are presented in Table S3.
390

391 **Single cell regulatory network inference using SCENIC**

392 Single cell regulatory network inference and clustering (SCENIC) [22] was used to infer transcription
393 factor (TF) networks active in SSPCs, IIFCs, osteoblasts and chondrocytes. Analysis was
394 performed using recommended parameters using the packages SCENIC v1.3.1, AUCell v1.16.0,

395 and RcisTarget v1.14 and the motif databases RcisTarget and GRNboost. SCENIC package was
396 used to perform regulon based tSNE clustering and identified population specific regulons.
397
398 **Cell-cell interaction using CellChat**
399 Cell communication analysis was performed using the R package CellChat[33] with default
400 parameters on the complete fracture combined dataset and on the subset of SSPCs, IIFCs,
401 osteoblasts and chondrocytes.
402
403 **STRING network analyses**
404 To assess protein-protein interaction network, we used the STRING v11.5 database[64]. To assess
405 interaction in the chondro-core, we performed the analysis on the chondro-core and chondro-
406 specific TFs identified in our analysis. For osteo-core analyses, we performed the analysis with
407 osteo-core genes and the most significant interactions.
408
409 **Histology and immunofluorescence**
410 Mouse samples were processed as previously described[57]. Tibias were collected and fixed in 4% PFA
411 (sc-281692, CliniSciences) for 4 hours at 4°C. Then, samples were decalcified in 19% EDTA for 10
412 days (EU00084, Euromedex), cryoprotected in 30% sucrose (200-301-B, Euromedex) for 24h and
413 embedded in OCT. Samples were sectioned in 10µm thick sections. Cryosections were defrosted
414 and rehydrated in PBS. For Safranin-O staining, sections were stained with Weigert's solution for
415 5 min, rinsed in running tap water for 3 min and stained with 0.02% Fast Green for 30 seconds
416 (F7252, Merck), followed by 1% acetic acid for 30 seconds and Safranin'O solution for 45 min
417 (S2255, Merck). For immunofluorescence, sections were incubated 1 hour at room temperature in
418 5% serum, 0.25% Triton PBS before incubation overnight at 4°C with the following antibodies: Rat
419 monoclonal to mouse SCA1 (740450, BD Biosciences), Rabbit monoclonal to mouse SOX9
420 (ab185230, Abcam), Rabbit polyclonal to mouse Osterix/Sp7 (ab22552, Abcam), Goat polyclonal
421 to mouse Periostin (AF2955, R&D Systems), Goat polyclonal to mouse PECAM1 (AF3628,
422 Biotechne), Rat monoclonal to mouse CD45 (552848, BD Bioscience). Secondary antibody

423 incubation was performed at room temperature for 1 hour. Slides were mounted with Fluoromount-
424 G mounting medium with DAPI (00-4959-52, Life Technologies).
425
426 **RNAscope in situ hybridization**
427 The expression of *Pi16* and *Postn* was visualized using the RNAscope® Multiplex Fluorescent
428 Assay V2 (Biotechne). Tissues were processed as described above. Ten µm thick sections were
429 cut and processed according to the manufacturer's protocol: 15 min of post-fixation in 4% PFA,
430 ethanol dehydration, 10 min of H_2O_2 treatment and incubation in ACD custom reagent for 30
431 minutes at 40°C. After hybridization and revelation, the sections were mounted under a glass
432 coverslip with Prolong Gold Antifade (P10144, ThermoFischer).
433
434 **Tissue dissociation and cell sorting**
435 *Periosteal SSPC isolation*
436 To isolate periosteal cells, uninjured tibias from *Prx1*^{Cre}*; R26*^{mTmG} mice were collected, and all
437 surrounding soft tissues were carefully removed. Epiphyses were embedded in low melting agarose and
438 tibias were placed for 30 at 37°C in digestion medium composed of PBS with 3mg/ml of Collagenase B
439 (C6885, Merck), 4mg/ml of Dispase (D4693, Merck) and 100U/mL of DNAse I (WOLS02007, Serlabo,
440 France). After digestion, tibias were removed and the suspension was filtered, centrifuged and
441 resuspended.
442
443 *Injury-induced fibrogenic cell isolation*
444 The fracture hematoma and the activated periosteum were collected from *Prx1*^{Cre}*; R26*^{mTmG} mice 3 days
445 post-fracture. Tissues were minced and digested at 37°C for 2 hours in DMEM (21063029, Life
446 Technologies) with 1% Trypsin (15090046, Life Technologies) and 1% collagenase D (11088866001,
447 Roche). Cells in suspension were removed every 20 min and the digestion medium was replaced. After
448 2 hours, the cell suspension was filtered, centrifuged and resuspended.
449
450 *Cell sorting and transplantation*
451 Digested cells were incubated 30 minutes with anti-SCA1-BV650 (BD Biosciences, 740450) or anti-
452 CD146-BV605 (BD Biosciences, 740636). Cells were sorted using Influx Cell Sorter. Prior sorting, Sytox

453 Blue (S34857, Thermo Fisher Scientific) was added to stain dead cells. We sorted living single GFP$^+$
454 SCA1$^+$ (pSSPCs excluding GFP$^-$ endothelial cells and SCA1$^-$ pericytes) and living single GFP$^+$ SCA1$^-$
455 cells from the uninjured periosteum of *Prx1^{Cre};Rosa^{mTmG}* mice. For IIFCs, living single GFP$^+$ CD146$^-$
456 cells were sorted, to eliminate CD146$^+$ pericytes. Cell transplantation was performed as described in [57].
457 30000 to 45000 sorted GFP$^+$ cells were embedded in Tisseel Prima fibrin gel, composed of fibrinogen
458 and thrombin (3400894252443, Baxter S.A.S, USA), according to manufacturer's instructions. Briefly,
459 the cells were resuspended in 15 µL of fibrin (diluted at 1/4), before adding 15 µL of thrombin (diluted at
460 1/4) and mixing. The pellet was then placed on ice for at least 15 min for polymerization. The cell pellet
461 was transplanted at the fracture site of wild-type mice at the time of fracture.
462

463 **In vitro colony-forming Unit (CFU) assay**

464 Prx1-GFP$^+$ SCA1$^+$ and Prx1-GFP$^+$ SCA1$^-$ periosteal cells were isolated from *Prx1^{Cre};Rosa^{mTmG}*
465 mice as described above. Sorted cells were plated at a cell density of 2000 cells per 6 well-plates
466 in growth media consisting of MEMα supplemented with 20% FBS, 1% penicillin-streptomycin (Life
467 Technology, Carlsbad, California), and 0.01% bFGF (R&D, Minneapolis, MN). The medium was
468 changed every 2-3 days. After 11 days, plates were washed twice with PBS, fixed with methanol,
469 stained with 0,5% crystal violet diluted in 20% methanol and colonies were manually counted.
470

471 **Statistical analyses**

472 Statistical difference between the number of activated regulons per cell was determined using one
473 way-ANOVA followed by a post-hoc test. A p-value < 0.001 is reported as ***.
474

475 ## Resource availability

476 Single nuclei RNAseq datasets are deposited in the Gene Expression Omnibus (GSE234451). The
477 integrated dataset was deposited on USCS Cell Browser for easy use: (https://fracture-repair-
478 atlas.cells.ucsc.edu). This paper does not report original code. Further information and requests for
479 resources and reagents should be directed to and will be fulfilled by the lead contact, Céline Colnot
480 (celine.colnot@inserm.fr).

481 ## Acknowledgements

482 This work was supported by ANR-18-CE14-0033, ANR-21-CE18-007-01, NIAMS R01 AR072707 and
483 R01 AR081671 to C.C. S. Perrin, M. Ethel and C. Goachet were supported by a PhD fellowship from
484 Paris Cité University, Univ Paris-Est Creteil and Fondation pour la Recherche Médicale respectively.
485 We thank O. Ruckebusch and A. Guigan from the Flow Cytometry platform at IMRB Institute, O. Pellé
486 from the Flow Cytometry platform at Imagine Institute and all the staff from the Imagine genomic core
487 facility at Imagine Institute. We thank A. Julien, S. Protic and Y. Hachemi for technical assistance or
488 advice.

489 ## Conflict of interests

490 Authors declare no competing interests.

491 ## Author contributions

492 Conceptualization: S.P. and C.C. Methodology: S.P. and C.C. Formal analysis: S.P. and C-A.W.
493 Investigation: S.P., M.E., V.B., C.G., M.L., F.C. and C.M. Resources: F.C. and M.M. Writing – Original
494 Draft: S.P. and C.C. Visualization: S.P. Supervision: C.C. Project administration: C.C. Funding
495 Acquisition: C.C
496

497 **References**

498 1. Duchamp de Lageneste, O. *et al.* Periosteum contains skeletal stem cells with high bone
499 regenerative potential controlled by Periostin. *Nat Commun* **9**, 773 (2018).
500 2. Jeffery, E. C., Mann, T. L. A., Pool, J. A., Zhao, Z. & Morrison, S. J. Bone marrow and periosteal
501 skeletal stem/progenitor cells make distinct contributions to bone maintenance and repair. *Cell Stem*
502 *Cell* **29**, 1547-1561.e6 (2022).
503 3. Julien, A. *et al.* Skeletal stem/progenitor cells in periosteum and skeletal muscle share a
504 common molecular response to bone injury. *J of Bone & Mineral Res* jbmr.4616 (2022)
505 doi:10.1002/jbmr.4616.
506 4. Julien, A. *et al.* Direct contribution of skeletal muscle mesenchymal progenitors to bone repair.
507 *Nature Communications* **12**, 2860 (2021).
508 5. Debnath, S. *et al.* Discovery of a periosteal stem cell mediating intramembranous bone
509 formation. *Nature* **562**, 133–139 (2018).
510 6. Matthews, B. G. *et al.* Heterogeneity of murine periosteum progenitors involved in fracture
511 healing. *eLife* **10**, e58534 (2021).
512 7. Ortinau, L. C. *et al.* Identification of Functionally Distinct Mx1+αSMA+ Periosteal Skeletal Stem
513 Cells. *Cell Stem Cell* **25**, 784-796.e5 (2019).
514 8. Matsushita, Y. *et al.* A Wnt-mediated transformation of the bone marrow stromal cell identity
515 orchestrates skeletal regeneration. *Nat Commun* **11**, 332 (2020).
516 9. De Micheli, A. J. *et al.* Single-Cell Analysis of the Muscle Stem Cell Hierarchy Identifies
517 Heterotypic Communication Signals Involved in Skeletal Muscle Regeneration. *Cell Rep* **30**, 3583-
518 3595.e5 (2020).
519 10. Guerrero-Juarez, C. F. *et al.* Single-cell analysis reveals fibroblast heterogeneity and myeloid-
520 derived adipocyte progenitors in murine skin wounds. *Nat Commun* **10**, 650 (2019).
521 11. Storer, M. A. *et al.* Acquisition of a Unique Mesenchymal Precursor-like Blastema State
522 Underlies Successful Adult Mammalian Digit Tip Regeneration. *Developmental Cell* **52**, 509-524.e9
523 (2020).
524 12. Sivaraj, K. K. *et al.* Mesenchymal stromal cell-derived septoclasts resorb cartilage during
525 developmental ossification and fracture healing. *Nat Commun* **13**, 571 (2022).
526 13. Machado, L. *et al.* Tissue damage induces a conserved stress response that initiates quiescent
527 muscle stem cell activation. *Cell Stem Cell* **28**, 1125-1135.e7 (2021).
528 14. Selewa, A. *et al.* Systematic Comparison of High-throughput Single-Cell and Single-Nucleus
529 Transcriptomes during Cardiomyocyte Differentiation. *Sci Rep* **10**, 1535 (2020).
530 15. Ding, J. *et al.* Systematic comparison of single-cell and single-nucleus RNA-sequencing
531 methods. *Nat Biotechnol* **38**, 737–746 (2020).
532 16. Wen, F., Tang, X., Xu, L. & Qu, H. Comparison of single-nucleus and single-cell transcriptomes
533 in hepatocellular carcinoma tissue. *Mol Med Rep* **26**, 339 (2022).
534 17. Tournaire, G. *et al.* Nestin-GFP transgene labels skeletal progenitors in the periosteum. *Bone*
535 **133**, 115259 (2020).
536 18. Gao, B. *et al.* Macrophage-lineage TRAP+ cells recruit periosteum-derived cells for periosteal
537 osteogenesis and regeneration. *Journal of Clinical Investigation* **129**, 2578–2594 (2019).
538 19. Chan, C. K. F. *et al.* Identification and Specification of the Mouse Skeletal Stem Cell. *Cell* **160**,
539 285–298 (2015).
540 20. He, X. *et al.* Sox9 positive periosteal cells in fracture repair of the adult mammalian long bone.
541 *Bone* **103**, 12–19 (2017).
542 21. Böhm, A.-M. *et al.* Activation of Skeletal Stem and Progenitor Cells for Bone Regeneration Is
543 Driven by PDGFRβ Signaling. *Developmental Cell* **51**, 236-254.e12 (2019).
544 22. Aibar, S. *et al.* SCENIC: single-cell regulatory network inference and clustering. *Nat Methods*
545 **14**, 1083–1086 (2017).
546 23. Leclerc, K. *et al.* Hox genes are crucial regulators of periosteal stem cell identity. *Development*
547 **150**, dev201391 (2023).
548 24. Nemec, S. *et al.* Pitx1 directly modulates the core limb development program to implement
549 hindlimb identity. *Development* **144**, 3325–3335 (2017).
550 25. Takahashi, K. & Yamanaka, S. Induction of pluripotent stem cells from mouse embryonic and
551 adult fibroblast cultures by defined factors. *Cell* **126**, 663–676 (2006).
552 26. Chen, H. *et al.* Activation of STAT6 by STING is critical for antiviral innate immunity. *Cell* **147**,
553 436–446 (2011).
554 27. Kollmann, S. *et al.* A STAT5B-CD9 axis determines self-renewal in hematopoietic and leukemic
555 stem cells. *Blood* **138**, 2347–2359 (2021).
556 28. Tsuruyama, T. *et al.* Dual retrovirus integration tagging: identification of new signaling molecules

557 Fiz1 and Hipk2 that are involved in the IL-7 signaling pathway in B lymphoblastic lymphomas. *J Leukoc*
558 *Biol* **88**, 107–116 (2010).
559 29. Le Grand, F. *et al.* Six1 regulates stem cell repair potential and self-renewal during skeletal
560 muscle regeneration. *J Cell Biol* **198**, 815–832 (2012).
561 30. Linares, A. J. *et al.* The splicing regulator PTBP1 controls the activity of the transcription factor
562 Pbx1 during neuronal differentiation. *eLife* **4**, e09268 (2015).
563 31. Rottkamp, C. A., Lobur, K. J., Wladyka, C. L., Lucky, A. K. & O'Gorman, S. Pbx3 is required for
564 normal locomotion and dorsal horn development. *Dev Biol* **314**, 23–39 (2008).
565 32. Wang, S. *et al.* Meis1 Controls the Differentiation of Eye Progenitor Cells and the Formation of
566 Posterior Poles during Planarian Regeneration. *Int J Mol Sci* **24**, 3505 (2023).
567 33. Jin, S. *et al.* Inference and analysis of cell-cell communication using CellChat. *Nat Commun* **12**,
568 1088 (2021).
569 34. Ding, J. *et al.* Systematic comparison of single-cell and single-nucleus RNA-sequencing
570 methods. *Nat Biotechnol* **38**, 737–746 (2020).
571 35. van den Brink, S. C. *et al.* Single-cell sequencing reveals dissociation-induced gene expression
572 in tissue subpopulations. *Nat Methods* **14**, 935–936 (2017).
573 36. Buechler, M. B. *et al.* Cross-tissue organization of the fibroblast lineage. *Nature* **593**, 575–579
574 (2021).
575 37. Wosczyna, M. N. *et al.* Mesenchymal Stromal Cells Are Required for Regeneration and
576 Homeostatic Maintenance of Skeletal Muscle. *Cell Rep* **27**, 2029-2035.e5 (2019).
577 38. Lee, S. *et al.* Notch-Wnt signal crosstalk regulates proliferation and differentiation of
578 osteoprogenitor cells during intramembranous bone healing. *npj Regen Med* **6**, 29 (2021).
579 39. Wang, C. *et al.* NOTCH signaling in skeletal progenitors is critical for fracture repair. *Journal of*
580 *Clinical Investigation* **126**, 1471–1481 (2016).
581 40. Dishowitz, M. I., Terkhorn, S. P., Bostic, S. A. & Hankenson, K. D. Notch signaling components
582 are upregulated during both endochondral and intramembranous bone regeneration. *Journal*
583 *Orthopaedic Research* **30**, 296–303 (2012).
584 41. Kraus, J. M. *et al.* Notch signaling enhances bone regeneration in the zebrafish mandible.
585 *Development* **149**, dev199995 (2022).
586 42. Matthews, B. G. *et al.* Analysis of αSMA-Labeled Progenitor Cell Commitment Identifies Notch
587 Signaling as an Important Pathway in Fracture Healing. *J Bone Miner Res* **29**, 1283–1294 (2014).
588 43. Novak, S. *et al.* Modulation of Notch1 signaling regulates bone fracture healing. *J Orthop Res*
589 **38**, 2350–2361 (2020).
590 44. Cao, J. *et al.* Notch signaling pathway promotes osteogenic differentiation of mesenchymal stem
591 cells by enhancing BMP9/Smad signaling. *International Journal of Molecular Medicine* **40**, 378–388
592 (2017).
593 45. Minear, S., Leucht, P., Miller, S. & Helms, J. A. rBMP represses Wnt signaling and influences
594 skeletal progenitor cell fate specification during bone repair. *J Bone Miner Res* **25**, 1196–1207 (2010).
595 46. Minear, S. *et al.* Wnt Proteins Promote Bone Regeneration. *Sci. Transl. Med.* **2**, (2010).
596 47. Kang, S. *et al.* Wnt Signaling Stimulates Osteoblastogenesis of Mesenchymal Precursors by
597 Suppressing CCAAT/Enhancer-binding Protein α and Peroxisome Proliferator-activated Receptor γ.
598 *Journal of Biological Chemistry* **282**, 14515–14524 (2007).
599 48. Komatsu, D. E. *et al.* Modulation of Wnt signaling influences fracture repair. *Journal Orthopaedic*
600 *Research* **28**, 928–936 (2010).
601 49. Chen, G. *et al.* The biological function of BMAL1 in skeleton development and disorders. *Life*
602 *Sciences* **253**, 117636 (2020).
603 50. Dudek, M. *et al. The clock transcription factor BMAL1 is a key regulator of extracellular matrix*
604 *homeostasis and cell fate in the intervertebral disc*.
605 http://biorxiv.org/lookup/doi/10.1101/2023.02.12.528214 (2023) doi:10.1101/2023.02.12.528214.
606 51. Dudek, M. *et al.* The chondrocyte clock gene Bmal1 controls cartilage homeostasis and integrity.
607 *Journal of Clinical Investigation* **126**, 365–376 (2015).
608 52. Ma, Z. *et al.* Deletion of clock gene Bmal1 impaired the chondrocyte function due to disruption
609 of the HIF1α-VEGF signaling pathway. *Cell Cycle* **18**, 1473–1489 (2019).
610 53. Takarada, T. *et al.* Clock Genes Influence Gene Expression in Growth Plate and Endochondral
611 Ossification in Mice. *Journal of Biological Chemistry* **287**, 36081–36095 (2012).
612 54. Xia, C. *et al.* TGF-β/Smad2 signalling regulates enchondral bone formation of Gli1 $^{+}$ periosteal
613 cells during fracture healing. *Cell Prolif* **53**, (2020).
614 55. Logan, M. *et al.* Expression of Cre recombinase in the developing mouse limb bud driven by
615 aPrxl enhancer. *genesis* **33**, 77–80 (2002).
616 56. Muzumdar, M. D., Tasic, B., Miyamichi, K., Li, L. & Luo, L. A global double-fluorescent Cre

617 reporter mouse. *Genesis* **45**, 593–605 (2007).
618 57. Perrin, S., Julien, A., Duchamp de Lageneste, O., Abou-Khalil, R. & Colnot, C. Mouse Periosteal
619 Cell Culture, in vitro Differentiation, and in vivo Transplantation in Tibial Fractures. *BIO-PROTOCOL* **11**,
620 (2021).
621 58. Santos, M. D. *et al.* Extraction and sequencing of single nuclei from murine skeletal muscles.
622 *STAR Protocols* **2**, 100694 (2021).
623 59. G Martelotto, L. *'Frankenstein' protocol for nuclei isolation from fresh and frozen tissue for*
624 *snRNAseq v2*. https://www.protocols.io/view/frankenstein-protocol-for-nuclei-isolation-from-f-3fkgjkw
625 (2019) doi:10.17504/protocols.io.3fkgjkw.
626 60. Stuart, T. *et al.* Comprehensive Integration of Single-Cell Data. *Cell* **177**, 1888-1902.e21 (2019).
627 61. Butler, A., Hoffman, P., Smibert, P., Papalexi, E. & Satija, R. Integrating single-cell
628 transcriptomic data across different conditions, technologies, and species. *Nat Biotechnol* **36**, 411–420
629 (2018).
630 62. Cao, J. *et al.* The single-cell transcriptional landscape of mammalian organogenesis. *Nature*
631 **566**, 496–502 (2019).
632 63. Kuleshov, M. V. *et al.* Enrichr: a comprehensive gene set enrichment analysis web server 2016
633 update. *Nucleic Acids Res* **44**, W90-97 (2016).
634 64. Szklarczyk, D. *et al.* The STRING database in 2021: customizable protein-protein networks, and
635 functional characterization of user-uploaded gene/measurement sets. *Nucleic Acids Res* **49**, D605–
636 D612 (2021).
637

638

Figures

Figure 1

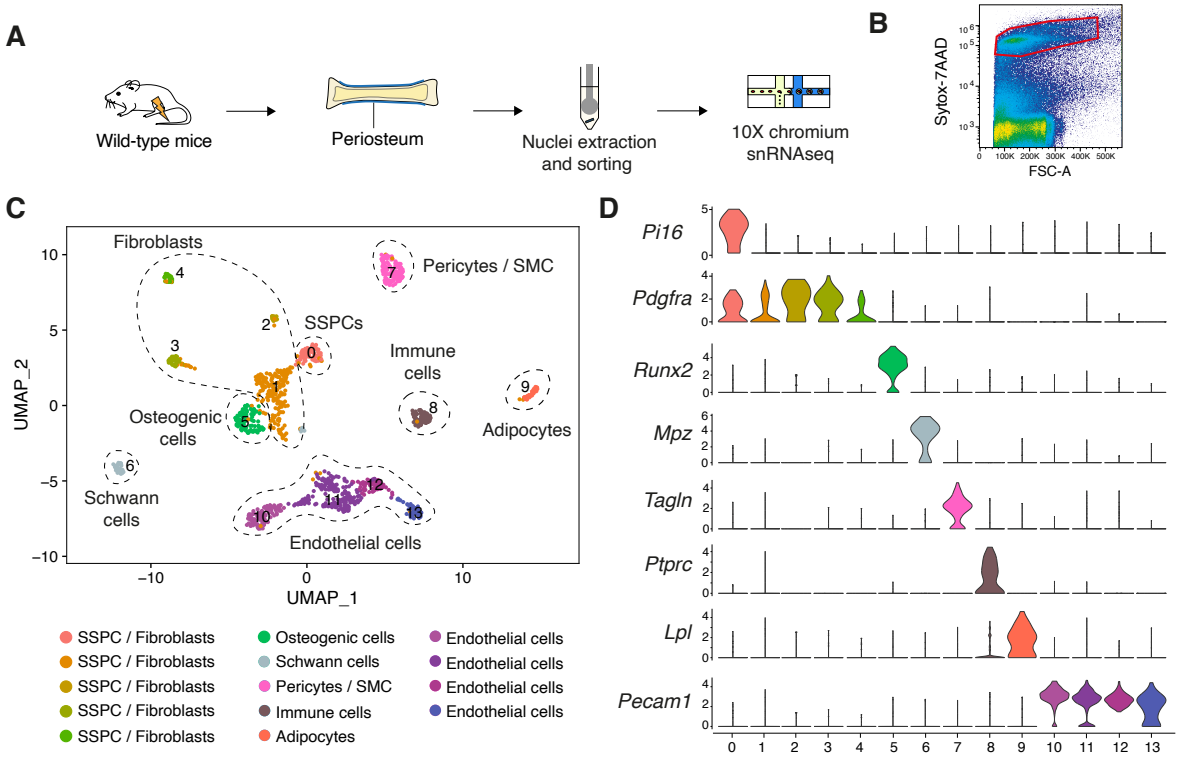

Figure 1: Heterogeneity of the periosteum at steady state

A. Experimental design. Nuclei were extracted from the periosteum of uninjured tibia and processed for single-nuclei RNAseq. **B.** Sorting strategy of nuclei stained with Sytox-7AAD for snRNAseq. Sorted nuclei are delimited by a red box. **C.** UMAP projection of color-coded clustering of the uninjured periosteum dataset. Six populations are identified and delimited by black dashed lines. **D.** Violin plots of key marker genes of the different cell populations.

Figure 2

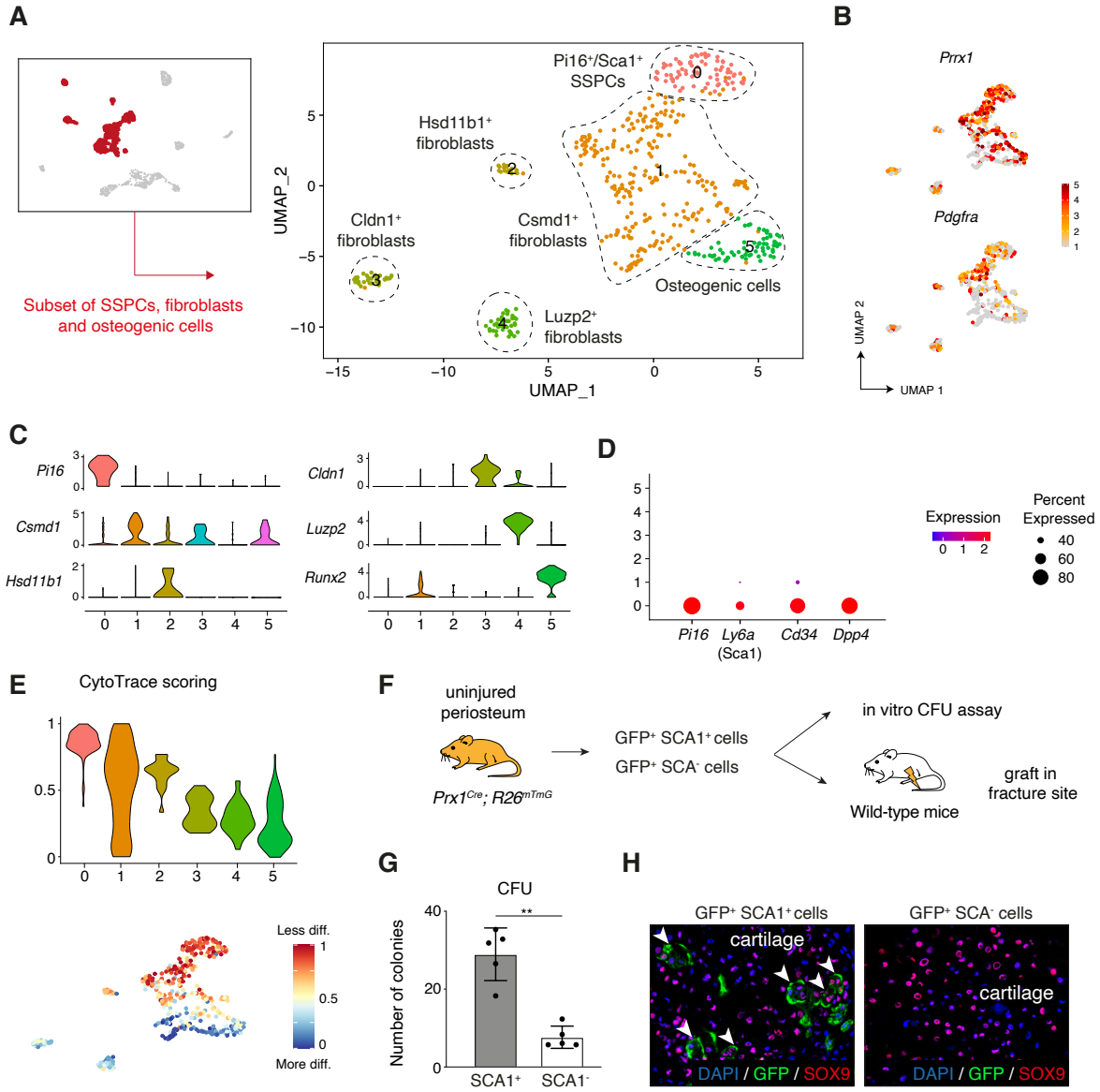

Figure 2: Identification of periosteal SSPCs in the intact periosteum

A. UMAP projection of color-coded clustering of the subset of SSPC/fibroblasts. **B.** Feature plots of *Prrx1* and *Pdgfra* in the subset of SSPC/fibroblasts. **C.** Feature plots of key marker genes of the different cell populations. **D.** Dot plot of the stemness markers *Pi16, Ly6a* (SCA1*), Cd34,* and *Dpp4*. **E.** Violin and feature plots of Cytotrace scoring in the subset of SSPC/fibroblasts, showing that SCA1⁺ SSPCs (cluster 0) are the less differentiated cells in the dataset. **F**. Experimental design: GFP⁺ SCA1⁺ and GFP⁺ SCA1⁻ were isolated from uninjured tibia of *Prx1*^{Cre}*; R26*^{mTmG} mice and used for in vitro CFU assays or grafted at the fracture site of wild-type mice. **G**. In vitro CFU assay of murine periosteal Prx1-GFP⁺ SCA1⁺ and Prx1-GFP⁺ SCA1⁻ cells. **H**. High magnification of SOX9 immunofluorescence of callus section 14 days

660 post-fracture showing that $GFP^{+}SCA1^{+}$ cells contribute to the callus (white arrowheads) while GFP^{+}

661 $SCA1^{-}$ cells are not contributing (n=3 per group).

662

Figure 3

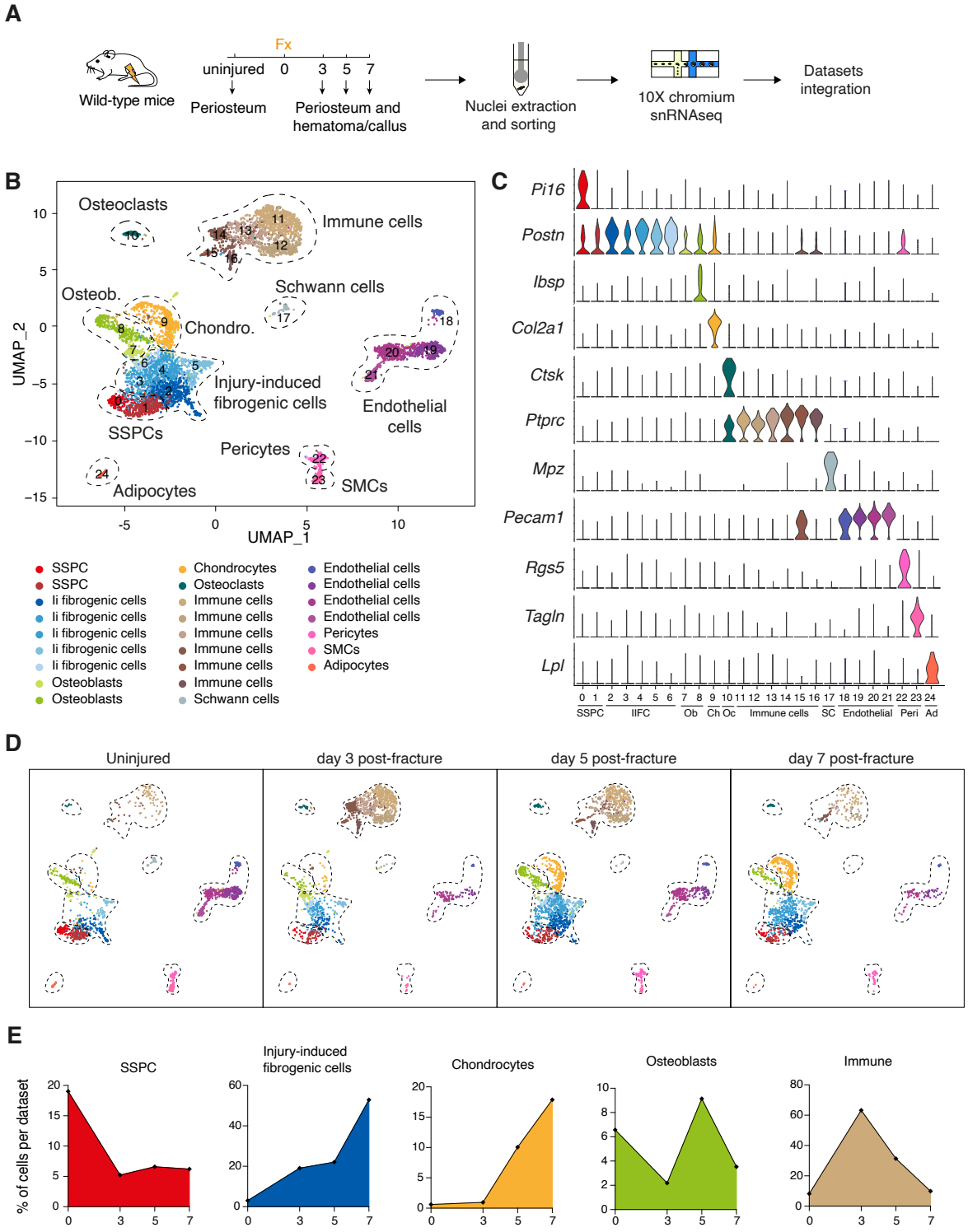
A
Wild-type mice
Fx
uninjured 0 3 5 7
Periosteum
Periosteum and hematoma/callus
Nuclei extraction and sorting
10X chromium snRNAseq
Datasets integration
B
Osteoclasts
Immune cells
Schwann cells
Osteob.
Chondro.
Injury-induced fibrogenic cells
Endothelial cells
SSPCs
Pericytes
SMCs
Adipocytes
UMAP_2
UMAP_1
SSPC
SSPC
Ii fibrogenic cells
Ii fibrogenic cells
Ii fibrogenic cells
Ii fibrogenic cells
Ii fibrogenic cells
Osteoblasts
Osteoblasts
Chondrocytes
Osteoclasts
Immune cells
Immune cells
Immune cells
Immune cells
Immune cells
Immune cells
Schwann cells
Endothelial cells
Endothelial cells
Endothelial cells
Endothelial cells
Pericytes
SMCs
Adipocytes
C
Pi16
Postn
Ibsp
Col2a1
Ctsk
Ptprc
Mpz
Pecam1
Rgs5
Tagln
Lpl
SSPC
IIFC
Ob
Ch
Oc
Immune cells
SC
Endothelial
Peri
Ad
D
Uninjured
day 3 post-fracture
day 5 post-fracture
day 7 post-fracture
E
SSPC
Injury-induced fibrogenic cells
Chondrocytes
Osteoblasts
Immune
% of cells per dataset

665

666 **Figure 3: Periosteal response to fracture at single-nuclei resolution**

667 **A.** Experimental design. Nuclei were extracted from the periosteum of uninjured tibia of wild-type mice
668 and from the injured periosteum and hematoma/callus at days 3, 5 and 7 post-tibial fracture and
669 processed for single-nuclei RNAseq. **B.** UMAP projection of color-coded clustering of the integration of
670 uninjured, day 3, day 5 and day 7 datasets. Eleven populations are identified and delimited by black
671 dashed lines. **C.** Violin plots of key marker genes of the different cell populations. **D.** UMAP projection
672 of the combined dataset separated by time-point. **E.** Percentage of cells in SSPC, injury-induced
673 fibrogenic cell, osteoblast, chondrocyte, and immune cell clusters in uninjured, day 3, day 5 and day 7
674 datasets.
675

Figure 4

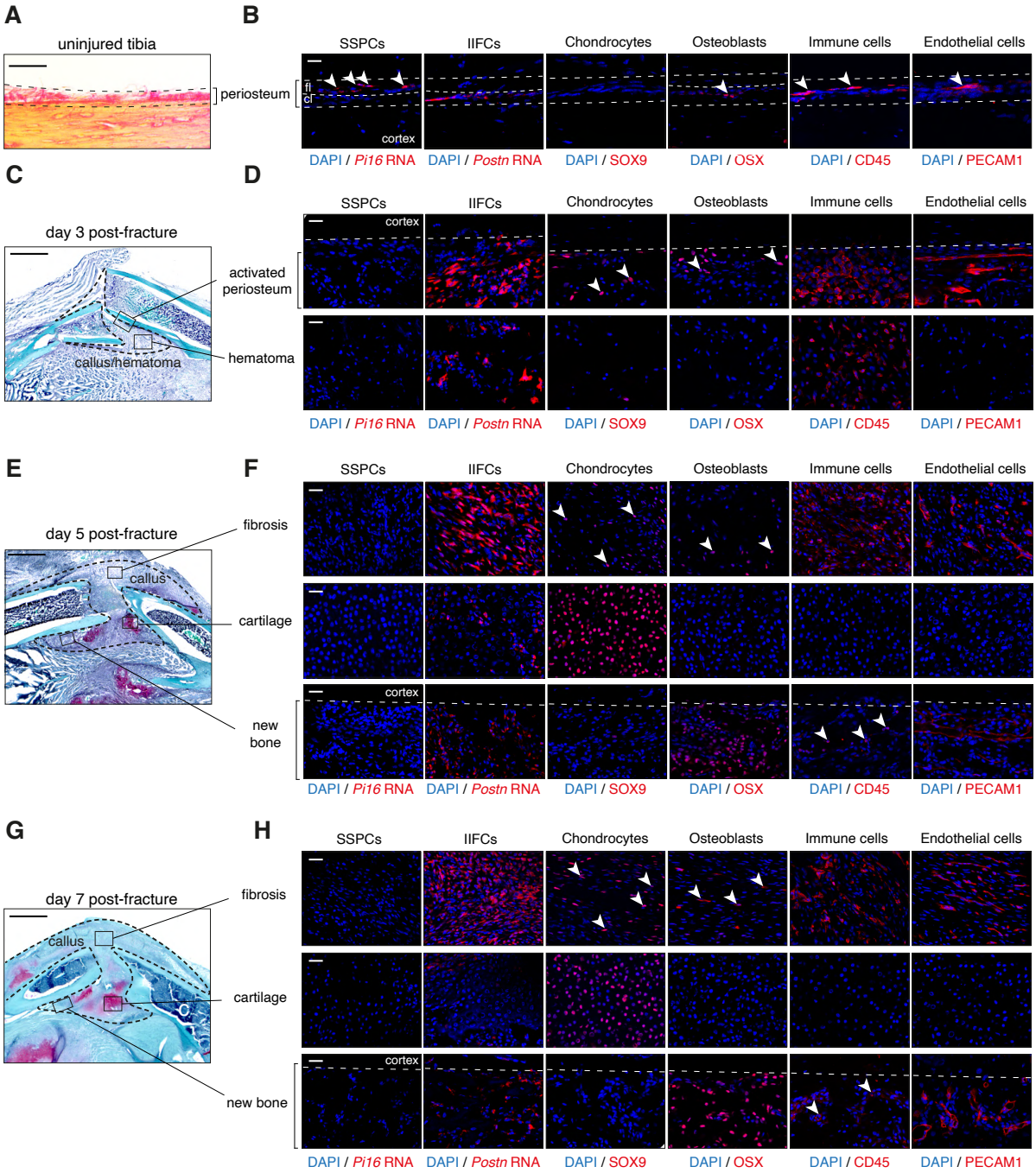

Figure 4: Cellular organization of the fracture callus

A. Picrosirius staining of the uninjured periosteum. **B**. Immunofluorescence and RNAscope on adjacent sections show the presence of SSPCs (*Pi16*-expressing cells) in the fibrous layer (fl), *Postn*-expressing cells in the cambium layer (cl), OSX^{+} osteoblasts, immune cells (CD45^{+}) and endothelial cells (PECAM1^{+}) in the periosteum (n=3 per group). **C.** Safranin'O staining of longitudinal callus sections at

682 day 3-post tibial fracture. **D**. Immunofluorescence and RNAscope on adjacent sections show absence
683 of SSPCs (*Pi16*$^{+}$), and presence of IIFCs (*Postn*$^{+}$) and immune cells (CD45^{+}) in the activated periosteum
684 and hematoma at day 3-post fracture. Chondrocytes (SOX9^{+},white arrowhead), osteoblasts (OSX^{+},white
685 arrowhead), immune cells (CD45^{+}) and endothelial cells (PECAM1^{+}) are detected in the activated
686 periosteum (n=3 per group). **E.** Safranin'O staining of longitudinal callus sections at day 5-post tibial
687 fracture. **F**. Immunofluorescence and RNAscope on adjacent sections show IIFCs (*Postn*$^{+}$),
688 chondrocytes (SOX9^{+}, white arrowhead), osteoblasts (OSX^{+},white arrowhead), immune cells (CD45^{+})
689 and endothelial cells (PECAM1^{+}) in the fibrosis, chondrocytes (SOX9^{+}) in the cartilage and osteoblasts
690 (OSX^{+}), immune cells (CD45^{+},white arrowhead) and endothelial cells (PECAM1^{+}) in the new bone. (n=3
691 per group). **G.** Safranin'O staining of longitudinal callus sections at day 7-post tibial fracture. **H**.
692 Immunofluorescence and RNAscope on adjacent sections show IIFCs (*Postn* $^{+}$), chondrocytes
693 (SOX9^{+},white arrowhead), osteoblasts (OSX^{+},white arrowhead), immune cells (CD45^{+}) and endothelial
694 cells (PECAM1^{+}) in the fibrosis, chondrocytes (SOX9^{+}) in the cartilage and osteoblasts (OSX^{+}), immune
695 cells (CD45^{+},white arrowhead) and endothelial cells (PECAM1^{+}) in the new bone (n=3 per group). Scale
696 bars: A-B-E: 1mm, B-D-F: 100μm.
697

Figure 5

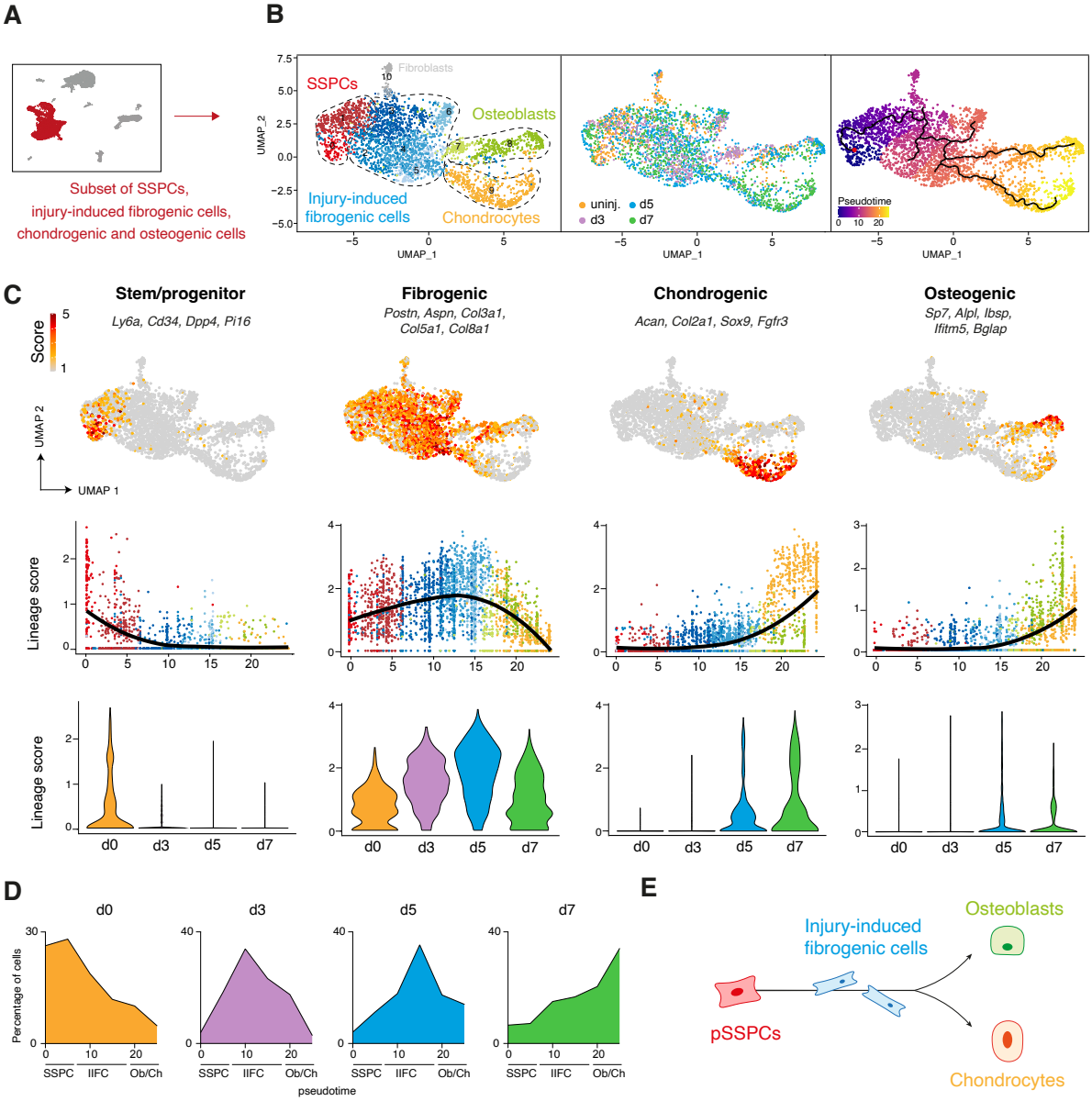

698

699

700 **Figure 5: Periosteal SSPCs activate through a common fibrogenic state prior to undergoing**

701 **osteogenesis or chondrogenesis**

702 **A.** SSPCs, injury-induced fibrogenic cells (IIFCs), chondrocytes and osteoblasts from integrated

703 uninjured, day 3, day 5 and day 7 post-fracture samples were extracted for a subset analysis. **B.** UMAP

704 projection of color-coded clustering (left), color-coded sampling (middle) and monocle pseudotime

705 trajectory (right) of the subset dataset. The four populations are delimited by black dashed lines. **C.** (top)

706 Feature plots of the stem/progenitor, fibrogenic, chondrogenic and osteogenic lineage scores (middle)

707 Scatter plot of the lineage scores along pseudotime. (bottom) Violin plot of the lineage score per time
708 point. **D.** Distribution of the cells along the pseudotime per timepoint. **E.** Schematic representation of the
709 activation trajectory of pSSPCs after fracture.
710

Figure 6

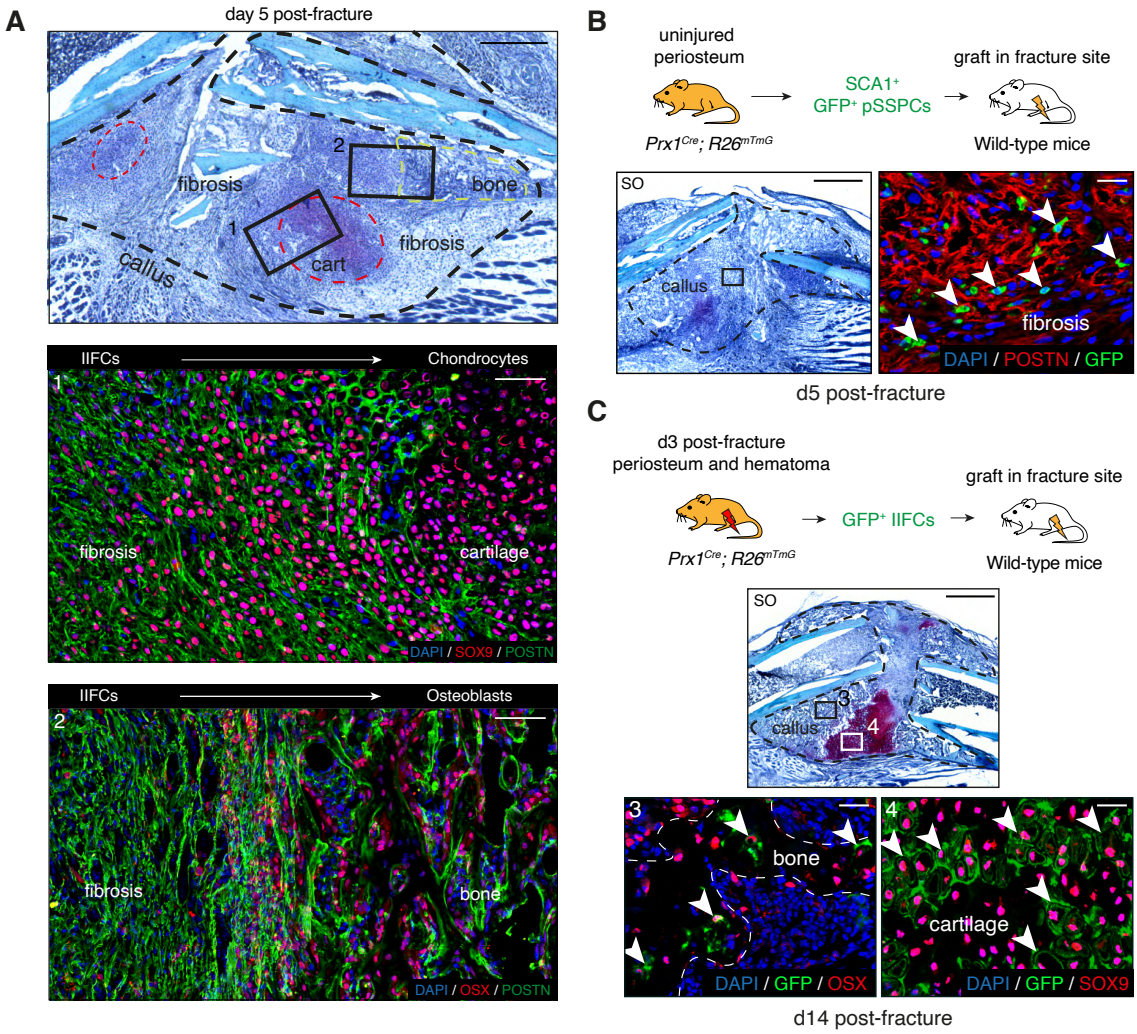

Figure 6: In vivo validation of pSSPC activation trajectory

A. (Top) Representative Safranin'O staining on longitudinal sections of the hematoma/callus at day 5 post-fracture. The callus is composed of fibrosis, cartilage (red dashed line) and bone (green dashed line). (Middle, box 1) Immunofluorescence on adjacent section shows decreased expression of POSTN (green) and increased expression of SOX9 (red) in the fibrosis-to-cartilage transition zone. (Bottom, box 2) Immunofluorescence on adjacent section shows decreased expression of POSTN (green) and increased expression of OSX (red) in the fibrosis-to-bone transition zone (n=3 per group). **B.** Experimental design: GFP$^+$ SCA1$^+$ SSPCs were isolated from uninjured tibia of *Prx1^{Cre}; R26^{mTmG}* mice and grafted at the fracture site of wild-type mice. Safranin'O staining of callus sections at day 5 post-fracture and high magnification of POSTN immunofluorescence of adjacent section showing that GFP$^+$

722 cells contribute to the callus and that grafted SSPCs differentiate into POSTN^{+} IIFCS (white arrowheads)
723 (n=4 per group). **C.** Experimental design: GFP^{+} IIFCs from periosteum and hematoma at day 3 post-
724 fracture tibia were isolated from *Prx1^{Cre}; R26^{mTmG}* mice and grafted at the fracture site of wild-type mice.
725 Safranin'O of callus sections at day 14 post-fracture and high magnification of OSX and SOX9
726 immunofluorescence of adjacent sections showing that GFP^{+} cells contribute to the callus and that
727 grafted IIFCs differentiate into OSX^{+} osteoblasts (box 3, white arrowheads) and SOX9^{+} chondrocytes
728 (box 4, white arrowheads) (n=4 per group). Scale bars: Low magnification: A: 500μm, B-C: 1mm. High
729 magnification: 100μm.
730

Figure 7

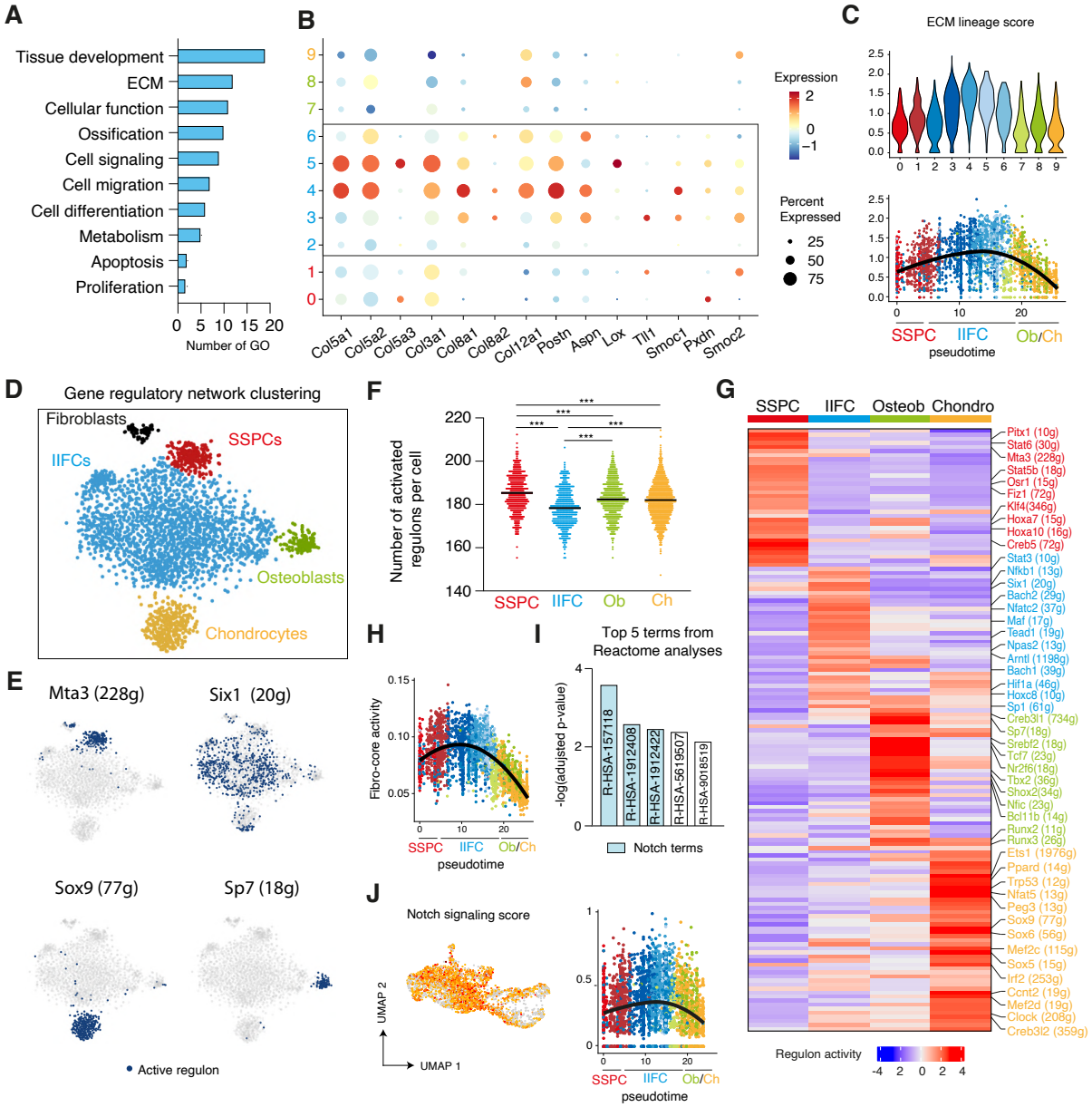

Figure 7: Characterization of injury-induced fibrogenic cells

A. Gene ontology analyses of upregulated genes in IIFCs (clusters 2 to 6 of UMAP clustering from Fig. 5). **B.** Dot plot of ECM genes in UMAP clustering from Fig. 5. **C.** Feature plot per cluster and scatter plot along pseudotime of the mean expression of ECM genes. **D.** Gene regulatory network (GRN)-based tSNE clustering of the subset of SSPCs, IIFCs, chondrocytes and osteoblasts. **E.** Activation of Mta3, Six1, Sox9 and Sp7 regulons in SSPCs, IIFCs, chondrocytes and osteoblasts. Blue dots mark cells with active regulon. **F.** Number of regulons activated per cell in the SSPC, IIFC, osteoblast (Ob) and chondrocyte (Ch) populations. Statistical differences were calculated using one-way ANOVA. ***: p-

741 value < 0.001. **G.** Heatmap of activated regulons in SSPC, IIFC, osteoblast (osteob) and chondrocyte
742 (chondro) populations. **H.** Scatter plot of the activity of the combined fibrogenic regulons along monocle
743 pseudotime from Fig. 5. **I.** Reactome pathway analyses of the fibrogenic regulons shows that the 3 most
744 significant terms are related to Notch signaling (blue). **J.** Feature plot in Seurat clustering and scatter
745 plot along monocle pseudotime of the Notch signaling score.
746

Figure 8

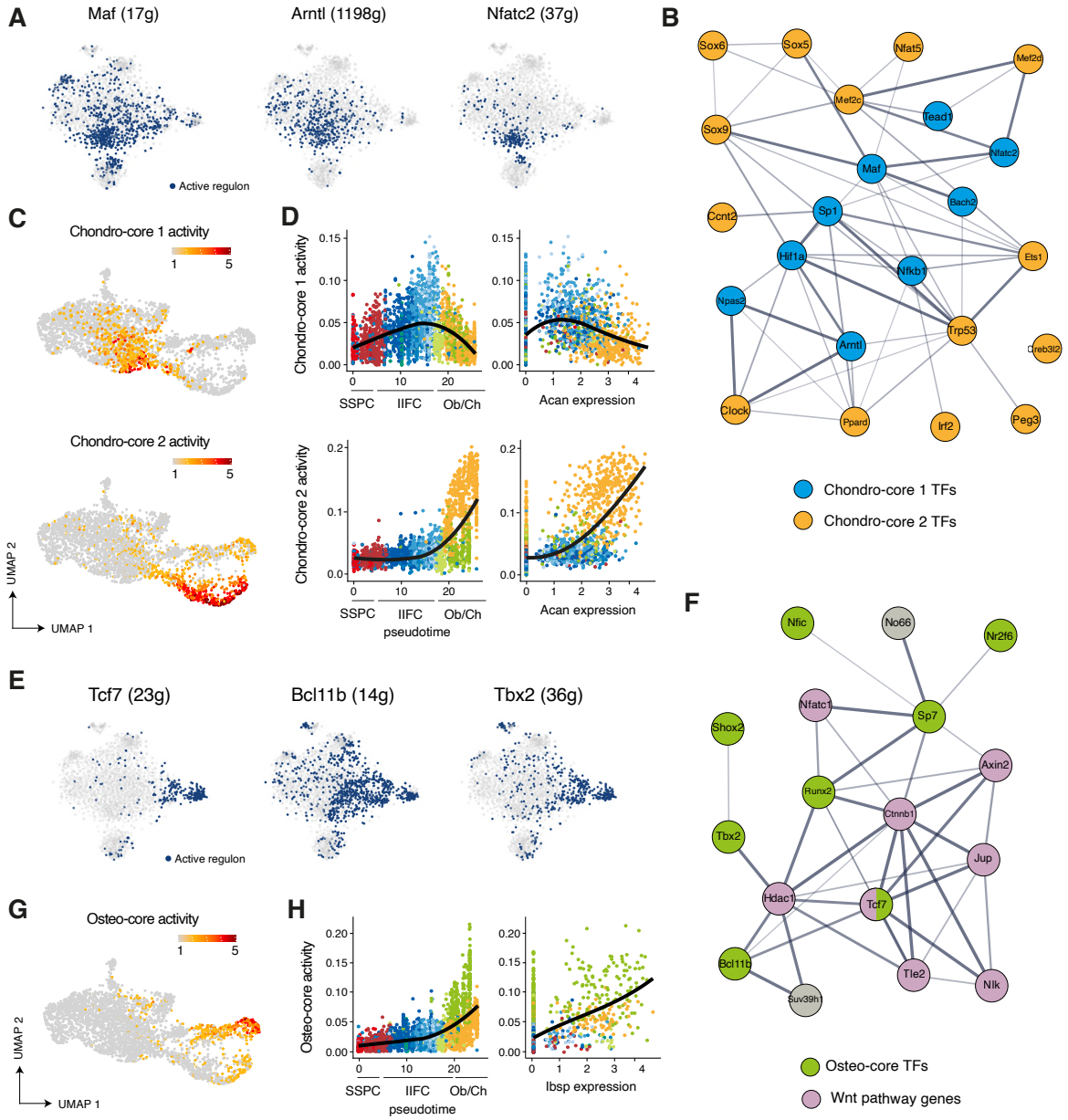

Figure 8: Gene regulatory network analyses identify gene cores driving fibrogenic to chondrogenic and osteogenic transitions.

A. Activation of Maf, Arntl, and Nfatc2 regulons in SSPCs, IIFCs, chondrocytes and osteoblasts. **B.** STRING interaction network of the chondro-core 1 and 2 transcription factors (blue and orange respectively). **C.** Feature plot of chondro-core 1 (top) and chondro-core 2 (bottom) activities in SSPCs, IIFCs, chondrocytes and osteoblasts in Seurat UMAP from Fig. 5. **D.** Scatter plot of chondro-core 1 (top) and chondro-core 2 (bottom) activities along monocle pseudotime and *Acan* expressing. **E.** Activation

756 of Tcf7, Bclb11b and Tbx2 regulons in SSPCs, IIFCs, chondrocytes and osteoblasts. **F**. STRING
757 interaction network of the osteo-core transcription factors (green) and their related genes shows that
758 most of osteo-core related genes are involved in Wnt pathway (purple). **G.** Feature plot of the osteo-
759 core activity in SSPCs, IIFCs, chondrocytes and osteoblasts in Seurat UMAP from Fig. 5. **H.** Scatter plot
760 of osteo-core activity along monocle pseudotime and *Ibsp* expressing.
761

Figure 9

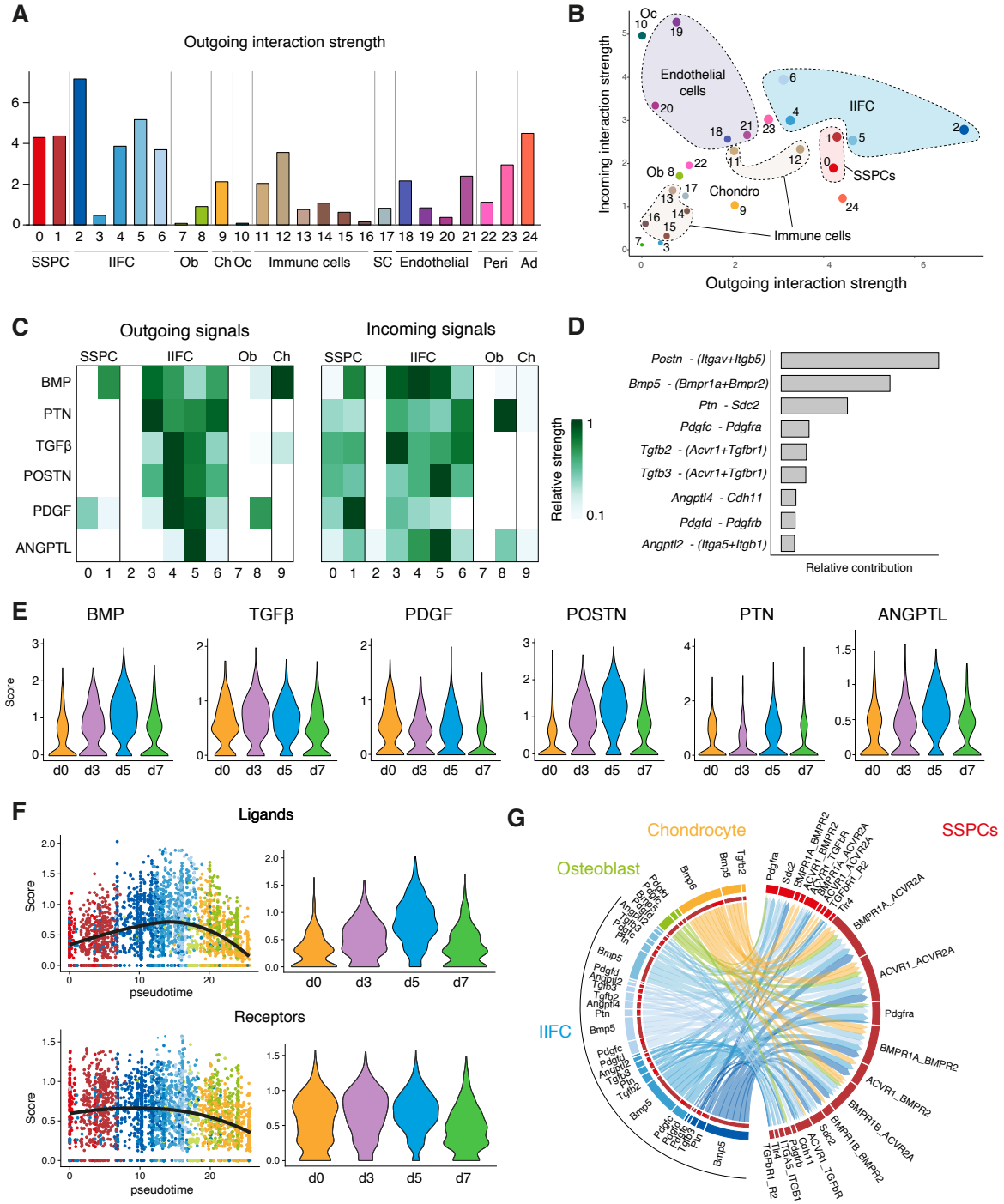

Figure 9: IIFCs are the main source of paracrine factors after fracture.

A. Outgoing interaction strengths of the different cell populations of the fracture environment determined using CellChat package. **B.** Comparison of incoming and outgoing interaction strengths across SSPC, IIFC, chondrogenic and osteogenic populations. **C.** Outgoing and incoming signaling from and to

767 SSPCs, IIFCs, chondrocytes and osteoblasts. **D.** Cell-cell interactions identified between SSPCs, IIFCs,
768 chondrocytes and osteoblasts. **E.** Violin plots of the score of BMP, TGFβ, PDGF, POSTN, PTN and
769 ANGPTL signaling per timepoint. **F.** Scatter plot along pseudotime and violin plot per time point of the
770 mean expression of the ligand and receptors involved in signaling from IIFCs. **G.** Circle plot of the
771 interactions between SSPCs, IIFCs, chondrocytes and osteoblasts, showing that most signals received
772 by SSPCs are coming for IIFCs. Ob: osteoblasts, Oc: osteoclasts, Ch: chondrocytes, SC: Schwann
773 cells, Ad: Adipocytes.
774

775 # Single nuclei transcriptomics reveal the differentiation trajectories

776 # of periosteal skeletal/stem progenitor cells in bone regeneration

777

778 **Supplemental information**

779

Figure 1 - Supplementary Figure 1

A

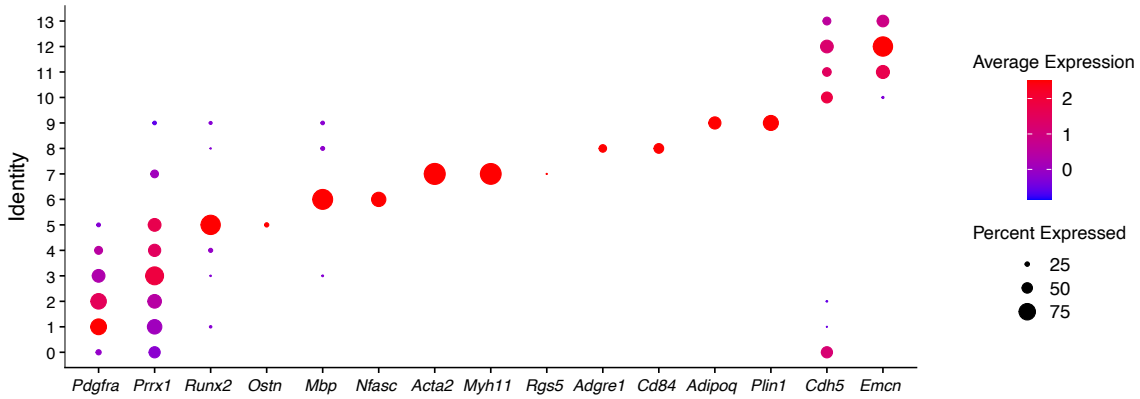

Figure 1 – Supplementary Figure 1A: Dot plot of marker genes of the populations from uninjured periosteum

Figure 2 - Supplementary Figure 1

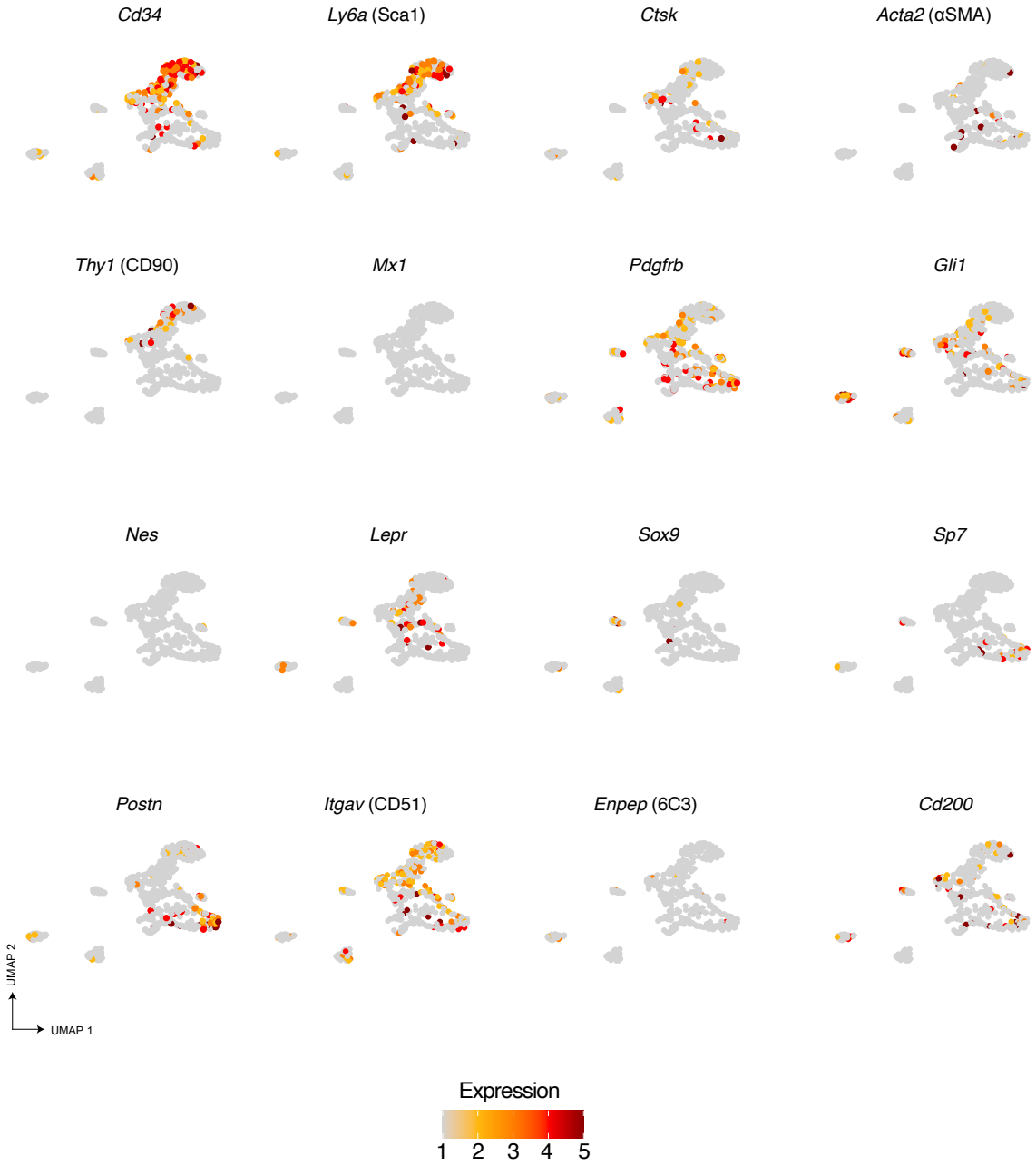

Figure 2 – Supplementary Figure 1: Expression of known SSPC markers in the periosteum at steady state.

Feature plots of known markers of SSPCs in the SSPC/fibroblast subset in periosteum at steady state.

Figure 3 - Supplementary Figure 1

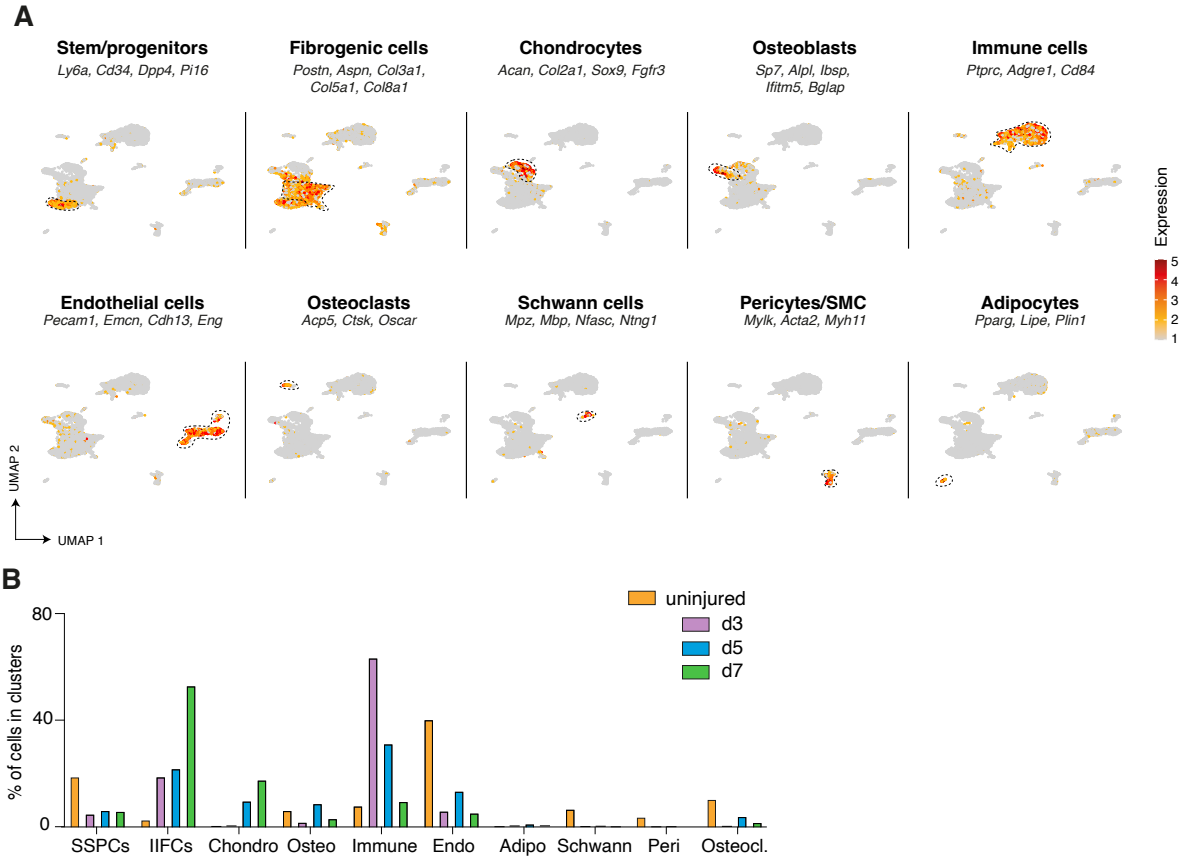

Figure 3 – Supplementary Figure 1 : Heterogeneity and dynamics of the cell populations in the fracture environment.

A. Feature plots of the lineage score of the different cell populations in the combined fracture datasets.

B. Percentage of cells in each cell population per time point.

Figure 3 - Supplementary Figure 2

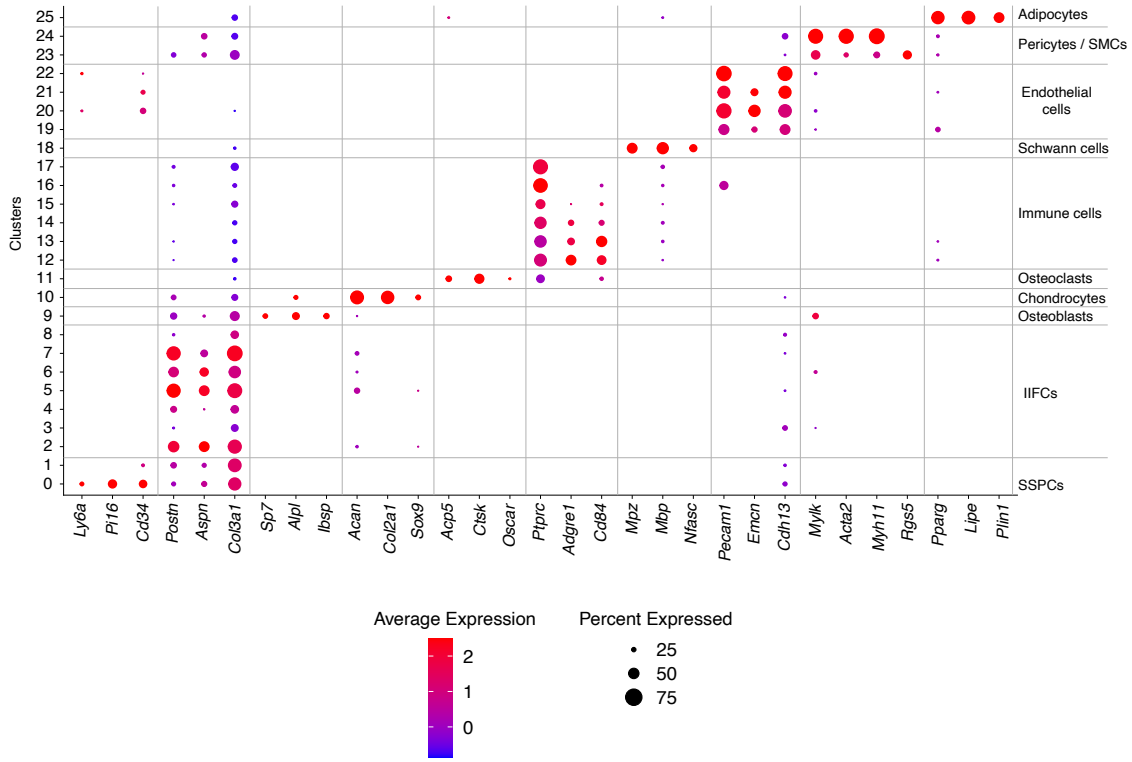

Figure 3 – Supplementary Figure 2: Dot plot of marker genes of the populations from the combined fracture dataset

Figure 4 - Supplementary Figure 1

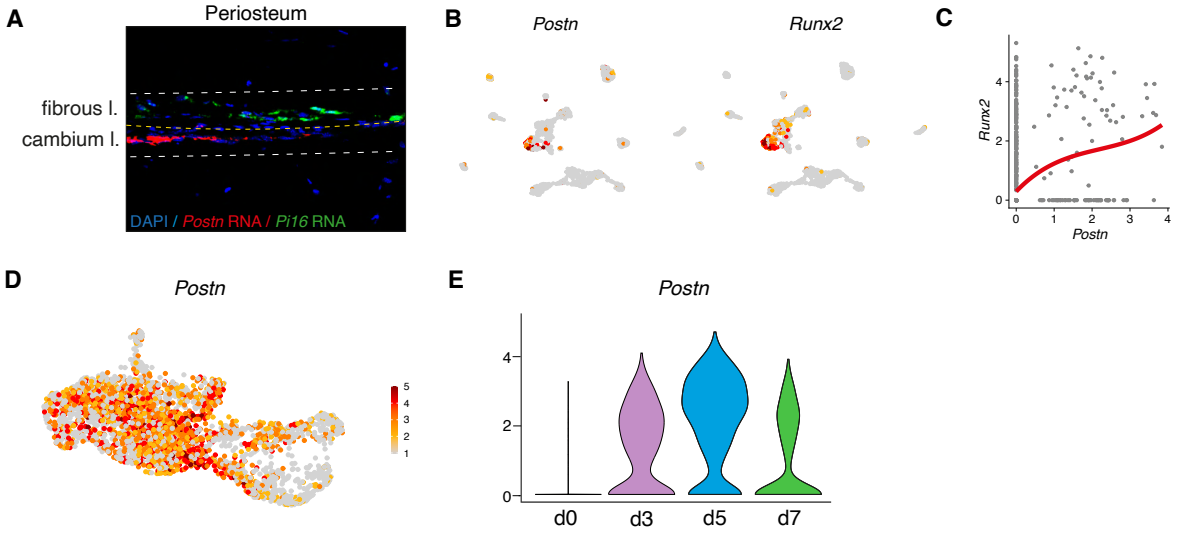

800

801 **Figure 4 – Supplementary Figure 1: Periosteal SSPCs do not express Postn**

802 **A.** RNAscope experiment showing the presence of *Postn* expressing cells in the inner cambium layer
803 (cl) of the periosteum and *Pi16*-expressing cells in the fibrous layer (fl). **B.** Feature plots of *Postn* and
804 *Runx2* expression in the uninjured periosteum. **B.** Scatter plot of *Runx2* and *Postn* expression in the
805 uninjured periosteum dataset showing that *Postn* is mostly expressed by cells expressing *Runx2*. **D.**
806 Feature plot of *Postn* expression in the subset of SSPCs, IIFCs, osteogenic and chondrogenic cells from
807 Fig. 5B. **E.** Violin plot of *Postn* expression per time point.

808

Figure 4 - Supplementary Figure 2

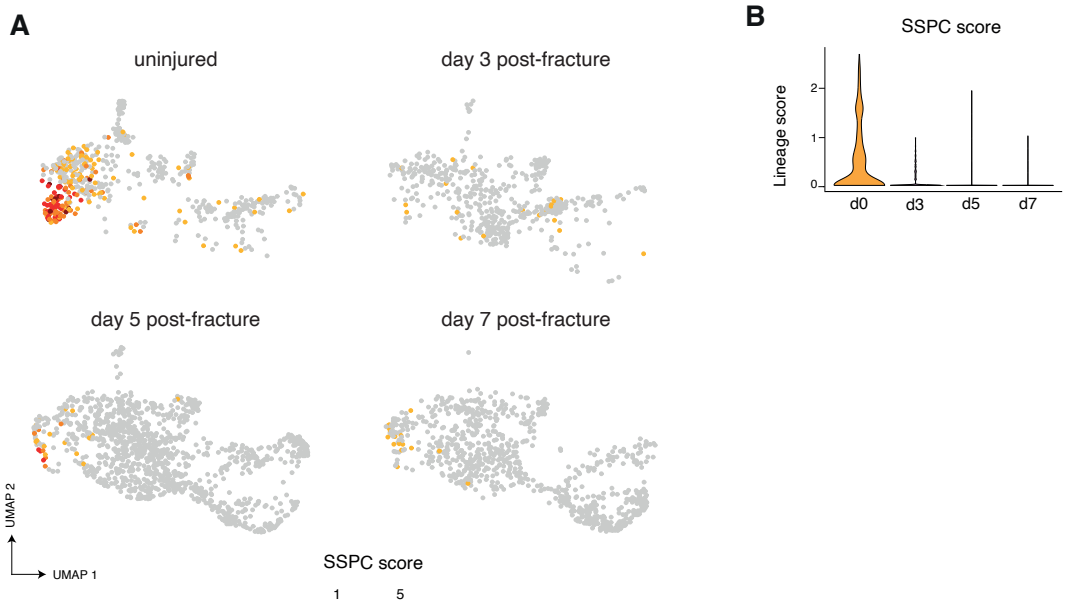

Figure 4 – Supplementary Figure 2: Absence of SSPCs in the injured periosteum.

A. Feature plot of SSPC lineage score in the subset of SSPCs, IIFCs, osteoblasts and chondrocytes separated by time point from Fig. 5B. **B**. Violin plot of SSPC lineage score by time point.

Figure 5 - Supplementary Figure 1

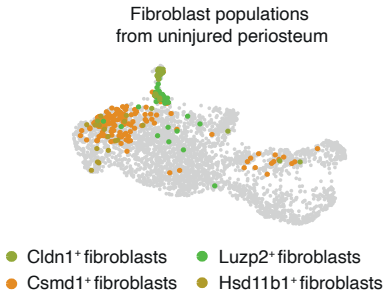

Figure 5 – Supplementary Figure 1: UMAP projection highlighting the distribution of periosteal fibroblasts in the combined fracture dataset.

Figure 6 - Supplementary Figure 1

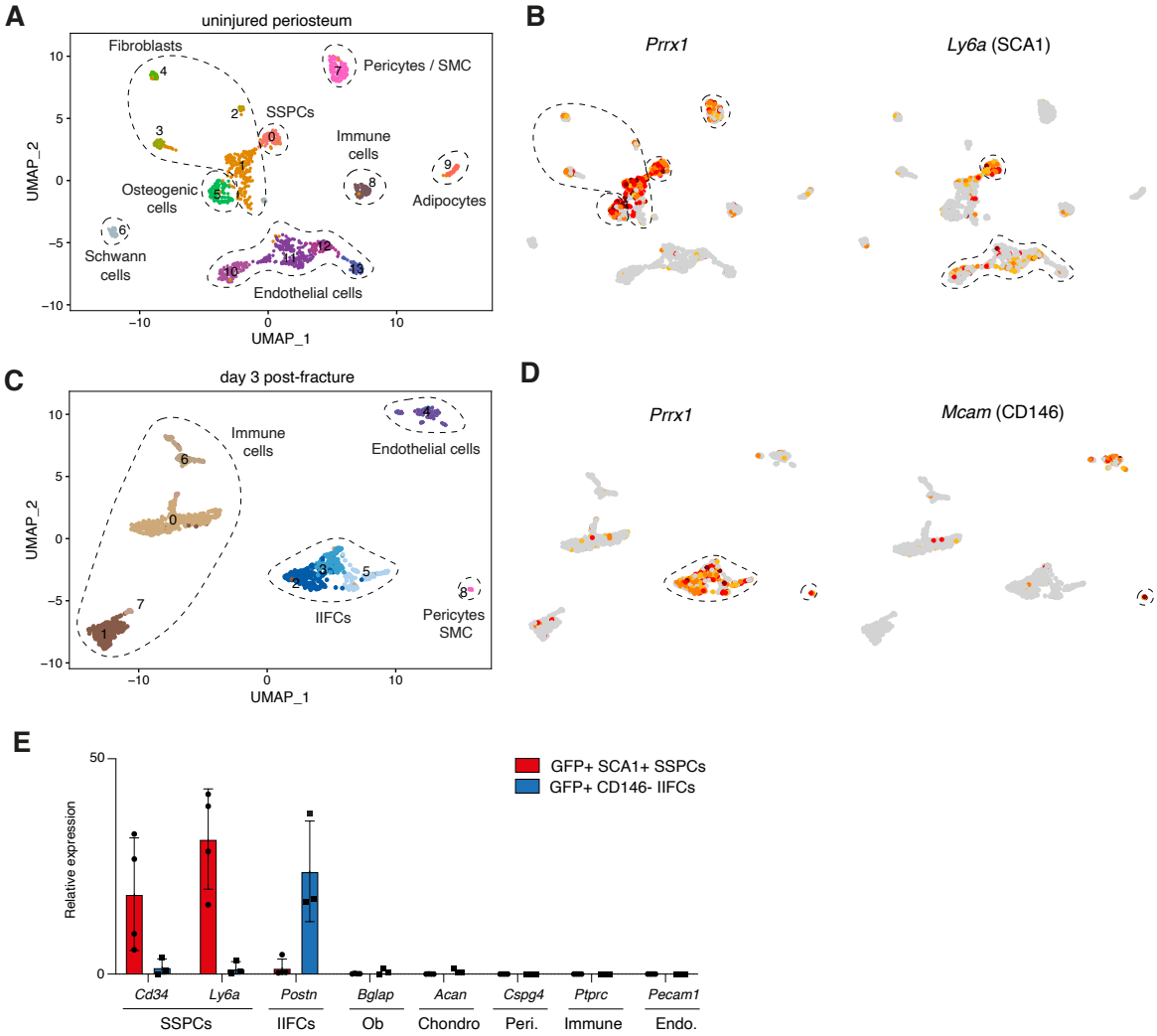

Figure 6 – Supplementary Figure 1: Validation of SSPC and IIFC sorting strategies.

A. UMAP projection of the clustering of the uninjured periosteum. **B**. Feature plots of Prxx1 and Ly6a expression in the uninjured dataset. **C**. UMAP projection of the clustering of the day 3 post-fracture periosteum and hematoma. **D.** Feature plots of Prxx1 and Mcam (CD146) expression in the day 3 post-fracture periosteum and hematoma dataset. **E**. Relative expression of cell population markers by Prx1^{+} SCA1^{+} SSPCs from uninjured periosteum and Prx1^{+} CD146^{-} IIFCs from day 3 post-fracture periosteum and hematoma.

Figure 7 - Supplementary Figure 1

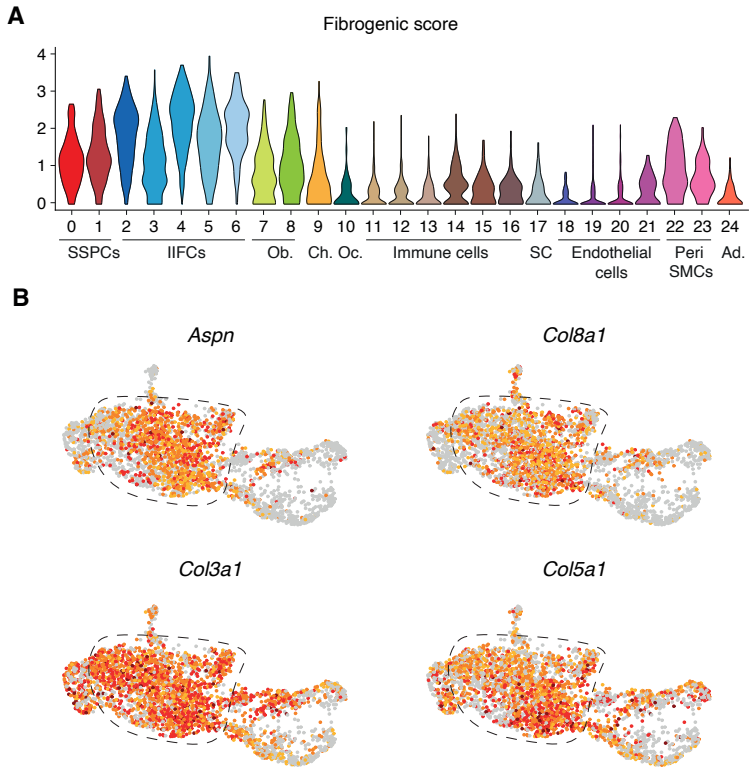

Figure 7 – Supplementary Figure 1: IIFCs are expressing ECM-related genes.

A. Violin plot of the extracellular matrix genes score in the integrated dataset. **B**. Feature plots of *Aspn, Col3a1, Col5a1* and *Col8a1* in the subset of SSPCs, IIFCs, osteoblasts and chondrocytes.

Figure 7 - Supplementary Figure 2

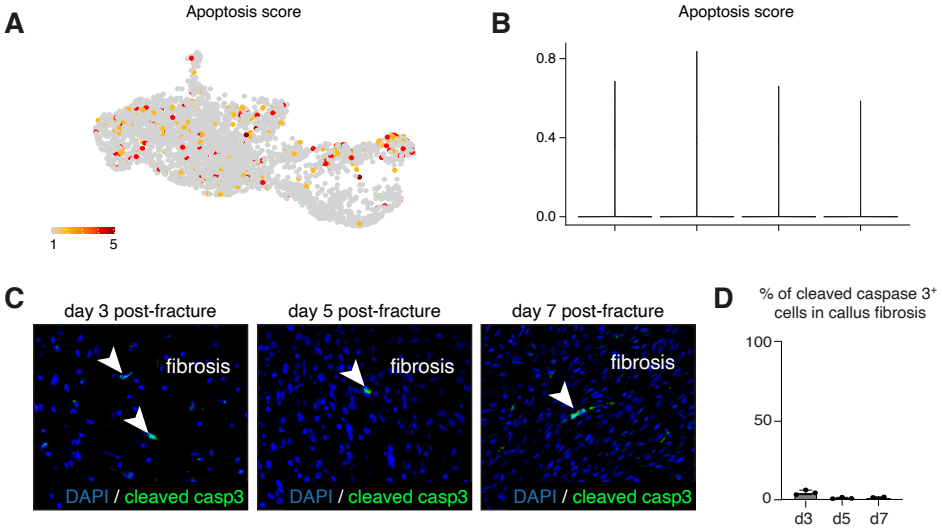

Figure 7 – Supplementary Figure 2: IIFCs do not undergo apoptosis.

A. Feature plot of the apoptosis score in the subset of SSPCs, IIFCs, osteoblast and chondrocytes. **B**. Violin plot of the apoptosis score separated by time points. **C**. Immunofluorescence of cleaved caspase 3 in callus fibrosis at day 3, 5 and 7 post-fracture. **D**. Percentage of cleaved caspase 3 positive cells in the fibrosis callus fibrosis at day 3, 5 and 7 post-fracture.

Figure 8 - Supplementary Figure 1

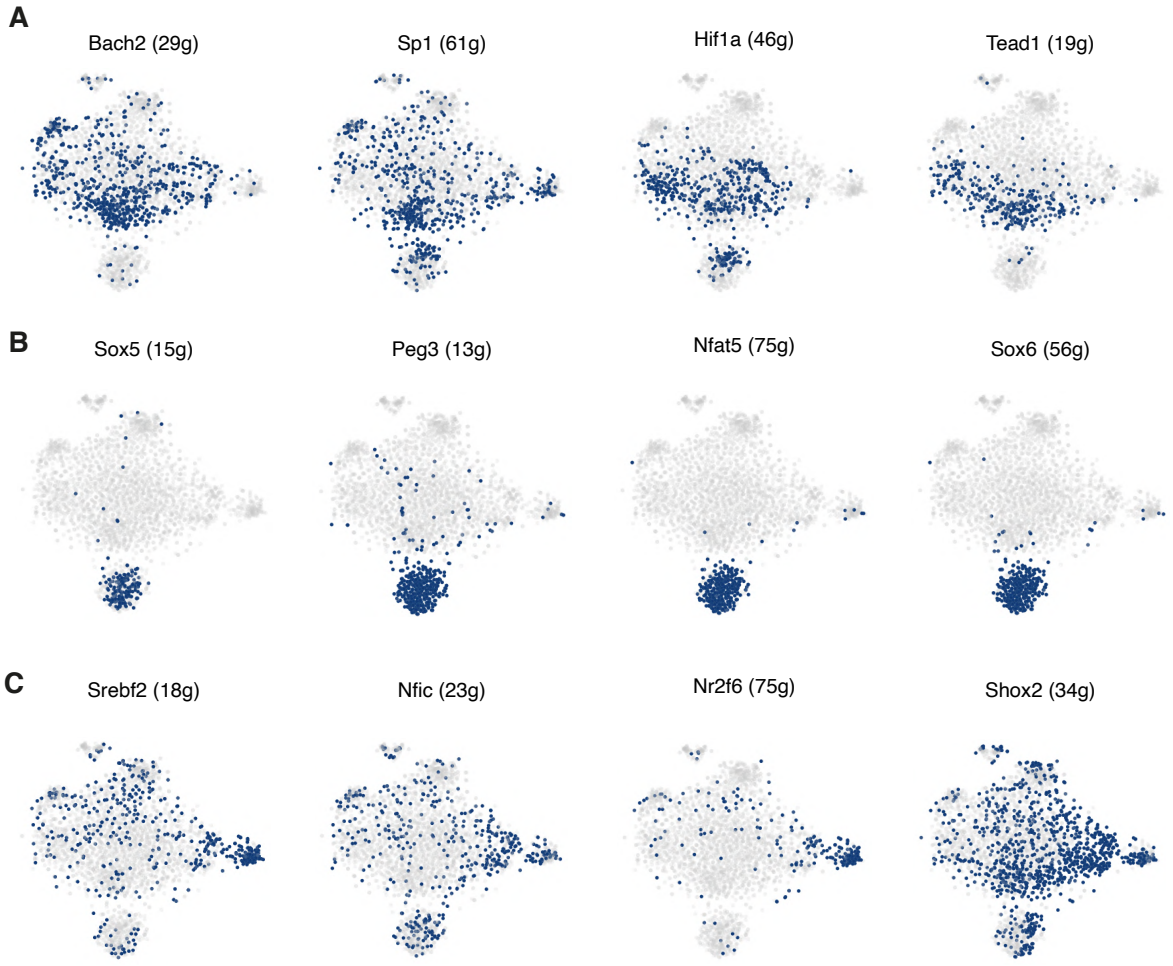

Figure 8 – Supplementary Figure 1: Regulon activity in the subset of SSPCs, IIFCs, osteoblasts and chondrocytes

A. Activity of Mta3, Six1, Sox9 and Sp7 regulons in the UMAP Seurat clustering of SSPCs, IIFCs, chondrocytes and osteoblasts. **B.** Activity of chondro-core 1 regulons in SCENIC tSNE clustering of SSPCs, IIFCs, chondrocytes and osteoblasts. **C.** Activity of chondro-core 2 regulons in SCENIC tSNE clustering of SSPCs, IIFCs, chondrocytes and osteoblasts. **D.** Activity of osteo-core regulons in SCENIC tSNE clustering of SSPCs, IIFCs, chondrocytes and osteoblasts.

Figure 9 - Supplementary Figure 1

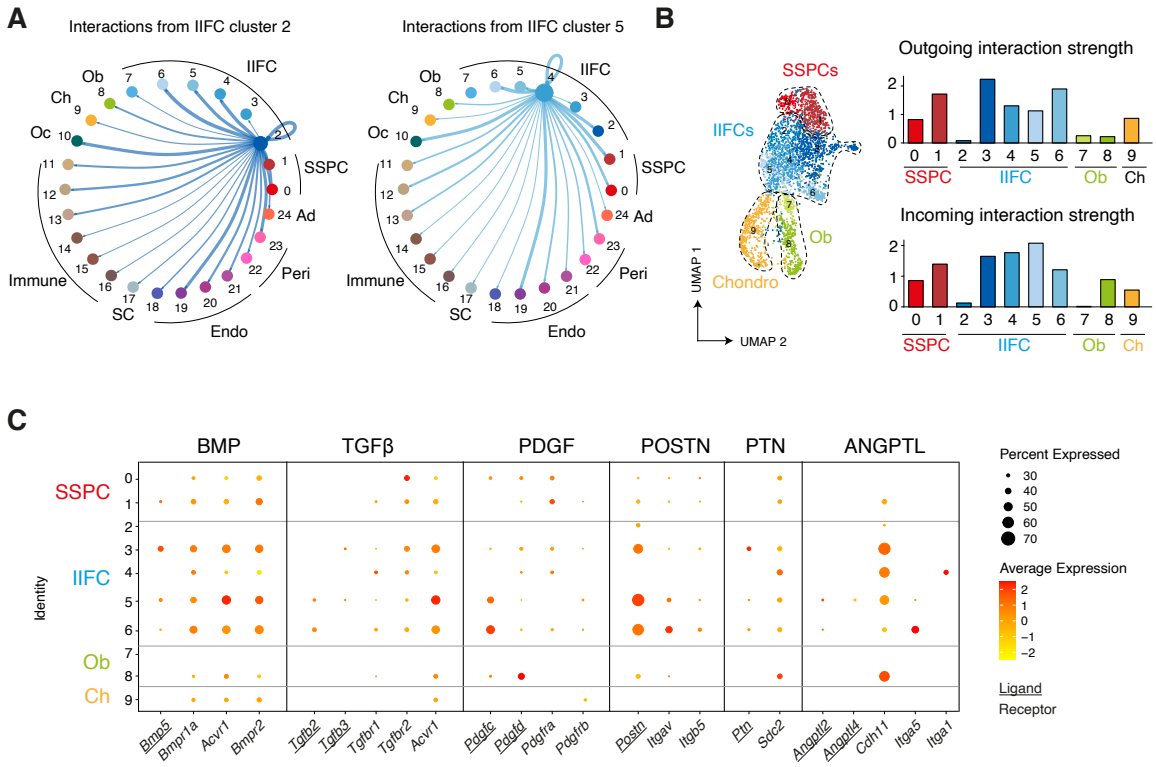

Figure 9 – Supplementary Figure 1: Paracrine interactions from IIFCs.

A. Circle plots showing the interaction strengths between IIFCs in clusters 2 and 5 with the other cell populations. **B.** (left) Feature plot of the subset of SSPCs, IIFCs, chondrocytes and osteoblasts from Fig 5. (right) Outgoing and incoming interaction strengths of the subset of SSPCs, IIFCs, chondrocytes and osteoblasts. **C.** Dot plots of the expression of the ligands (underlined) and receptors of BMP, TGFβ, PDGF, POSTN, PTN and ANGPTL family involved in cell-cell interactions from IIFCs after fracture.

Score	Genes
Stem/progenitor score	*Ly6a, Cd34, Dpp4, Pi16*
Fibrogenic score	*Postn, Aspn, Col3a1, Col5a1, Col8a1*
Chondrogenic score	*Acan, Col2a1, Sox9, Fgfr3*
Osteogenic score	*Sp7, Alpl, Ibsp, Ifitm5, Bglap*
Notch score	*Notch1, Notch3, Notch2, Notch4, Jag1, Dtx3, Fbxw7, Psen1, Epn2, Sel1l, Maml1, Spen, Anxa4*
ECM score	*Col5a1, Col5a2, Col5a3, Col3a1, Col8a1, Col8a2, Col12a1, Eln, Postn, Aspn, Lox, Tll1, Smoc1, Pxdn, Smoc2*
BMP score	*Bmp5, Bmpr1a, Acvr1, Bmpr2*
TGFb score	*Tgfb2, Tgfb3, Tgfbr1, Tgfbr2, Acvr1*
PDGF score	*Pdgfc, Pdgfd, Pdgfra, Pdgfrb*
POSTN score	*Postn, Itgav, Itgb5*
PTN score	*Ptn, Sdc2*
ANGPLT score	*Angptl2, Angptl4, Cdh11, Itga1, Itga5*
Total ligand score	*Bmp5, Tgfb2, Tgfb3, Postn, Ptn, Angptl4, Angptl2, Pdgfc, Pdgfd*
Total receptor score	*Bmpr1a, Acvr1, Bmpr2, Tgfbr1, Tgfbr2, Itgav, Itgb5, Sdc2, Ncl, Pdgfra, Pdgfrb*

861

862 **Table S1: Lists of genes used for lineage score analyses of murine snRNAseq.**

863

864

865

Group of regulons	Regulons
Fibro-core regulons	Arnt, Bach1, Bcl3, Cux1, E2f3, Elk4, Etv6, Fosl2, Foxn3, Foxp1, Jun, Junb, Mdb4, Meis1, Myc, Nfib, Pbx1, Pbx3, Rocor1, Runx1, Six1
Chondro-core 1 regulons	Npas2, Hif1a, Sp1, Arntl, Bach2, Nfkb1, Maf, Tead1, Nfatc2
Chondro-core 2 regulons	Sox6, Sox5, Sox9, Mef2c, Nfat5, Mef2d, Ccnt2, Clock, Ppard, Irf2, Trp53, Peg3, Creb3l2, Ets1
Osteo-core regulons	Nr2f6, Nfic, Shox2, Tbx2, Sp7, Bcl11b, Tcf7, Runx2

866

867 **Table S2: Lists of the regulons composing the cores.**

868

869

Reactome number	Term	Adjusted p-value
R-HSA-157118	Signaling By NOTCH	2,52E-04
R-HSA-1912408	Pre-NOTCH Transcription And Translation	0,00250164
R-HSA-1912422	Pre-NOTCH Expression And Processing	0,00331873
R-HSA-5619507	Activation Of HOX Genes During Differentiation	0,00394002
R-HSA-9018519	Estrogen-dependent Gene Expression	0,00697148

870

871 **Table S3: Top 5 terms from Reactome analysis on fibro-core regulons.**

872